Thesis for the degree of Licentiate of Engineering

Reaction kinetics of NH_3-SCR over Cu-CHA from first principles

Yingxin Feng

CHALMERS

Department of Physics
Chalmers University of Technology
Göteborg, Sweden 2021

Reaction kinetics of NH_3-SCR over Cu-CHA from first principles
Yingxin Feng

Thesis for the degree of Licentiate of Engineering 2021

Department of Physics
Chalmers University of Technology
SE-412 96 Göteborg
Sweden
Telephone: +46 (0)31-772 1000

Cover:
Simulated TOF from a first principles microkinetic model that include N_2O formation.

Printed at Chalmers Digitaltryck
Göteborg, Sweden 2021

Reaction kinetics of NH_3-SCR over Cu-CHA from first principles

Yingxin Feng
Department of Physics
Chalmers University of Technology

Abstract

Ammonia assisted selective catalytic reduction (NH_3-SCR) is a leading technology that is used for NO_x reduction to N_2 and H_2O in oxygen excess. Thanks to its high activity, high selectivity, and durability, Cu-CHA is commercialized as an NH_3-SCR catalyst. Despite the superior catalytic performance, small amounts of nitrous oxide (N_2O) are formed during the NH_3-SCR as an unwanted by-product. N_2O has a strong greenhouse potential and should be avoided. To further enhance the performance of NH_3-SCR catalysts to handle the increasingly stringent emission standards, understanding the mechanism for NH_3-SCR and, in particular, N_2O formation over Cu-CHA is essential.

In this thesis, density functional theory (DFT) calculations and first principles microkinetic simulations are used to investigate the reaction path and the reaction kinetics for low temperature-NH_3-SCR. Based on a previously proposed catalytic cycle for NH_3-SCR over Cu-CHA, an N_2O formation path is put forward. It is proposed that N_2O can form over linear $[Cu(NH_3)_2]^+$ complexes, which are present during low temperature operation. N_2O is formed from H_2NNO, which is generated via NH_2-NO coupling over a Cu-OOH-Cu site. The reaction proceeds with a low barrier and rationalizes the low-temperature N_2O emission peak observed experimentally at high Cu-loadings. N_2O formation at high temperatures is instead proposed to occur through the decomposition of NH_4NO_3.

With a catalytic cycle including N_2O formation, a first principles microkinetic model is developed to investigate the reaction kinetics of NH_3-SCR over Cu-CHA. When developing the model, special attention is paid assessing the change in entropy for each reaction step. The results from the kinetic model show good agreement with the experimental data of apparent activation energies, reaction orders and N_2O selectivity. The model links the catalytic performance with structure and forms the basis for further developments of the NH_3-SCR technology.

Keywords: Catalysis, density functional theory, microkinetic modeling, Cu-CHA, ammonia assisted selective catalytic reduction

People can do hard things.

List of Publications

This thesis is based on the following appended papers:

I. The Role of H^+- and Cu^+-Sites for N_2O Formation during NH_3-SCR over Cu-CHA
Y. Feng, T.V.W. Janssens, P.N.R. Vennestrøm, J. Jansson, M. Skoglundh and H. Grönbeck
The Journal of Physical Chemistry C, **125** (2021), 4595-4601

II. A First-Principles Microkinetic Model for Low-Temperature NH_3 Assisted Selective Catalytic Reduction of NO over Cu-CHA
Y. Feng, X. Wang, T.V.W. Janssens, P.N.R. Vennestrøm, J. Jansson, M. Skoglundh and H. Grönbeck
ACS Catalysis, Accepted

My contributions to the publications

Paper I
I performed all the calculations. I wrote the first draft of the paper, which was finalized together with my coauthors.

Paper II
I programmed the code for the mircokinetic modelling and performed all calculations. I wrote the first draft of the paper, which was finalized together with my coauthors.

Contents

Chapter 1

Introduction

Our society relies on efficient transportation of people and goods. At present, the transportation system is based mainly on combustion of liquid fossil fuels.[1] However, the extensive used of combustion engines is connected to emission of pollutants, such as nitrous oxide (NO_x), hydrocarbons (HC), and carbon monoxide (CO) that need to be controlled.[2] Moreover, combustion of carbon-based fuels results in carbon dioxide (CO_2) that is a greenhouse gas.[3] Thus, within a carbon-based transportation system, the fuel efficiency should be enhanced in order to reduce CO_2 emission. Thanks to the progress of engine technology, the emissions of modern engines have been greatly reduced as compared to the 1970s.[4–6] More importantly, the utilization of aftertreatment technologies has played an integral role to further reduce the emissions.[6;7] The current challenge within aftertreatment research is to meet increasingly rigorous emission standards,[8] and simultaneity improve the fuel efficiency.[6]

One current dominant technology that is used in the aftertreatment systems is the three-way catalyst (TWC). The application of TWC was a huge step forward for the emission control of gasoline engines. With the TWC, CO and HC in the emissions are oxidized to CO_2 and H_2O, while the NO_x is reduced to N_2.[9;10] In a typical TWC, the reactions occur over nanoparticles of noble metals, composed of Pt, Pd, and Rh, where CeO_2–ZrO_2 mixed oxides are added to play the role of oxygen storage materials and promoters.[11] To provided a high surface area, Al_2O_3 is employed as a support and barium and/or lanthana oxides are added to stabilize the surface area of Al_2O_3.[11] TWC has an obvious deficiency in that, it needs to operate under stoichiometric conditions, which limits the fuel efficiency.

In recent years, lean-burn engines have been widely used owing to their higher fuel efficiency.[9] Under the lean-burn condition with high air/fuel ratios, most of the fuel can be fully combusted into CO_2 and only release a minimal amount of CO and HC. However the challenge is that, the high temperature during the combustion will inevitably oxidize nitrogen in the air to NO_x. Therefore, there is an urgent need for catalysts that can selectively reduce NO_x in oxygen excess.

Currently, an efficient technology for NO_x reduction in oxygen excess is ammonia assisted selective catalytic reduction (NH_3-SCR),[12] which can reduce NO_x into N_2 and water.

1.1 Heterogeneous catalysis

In general, catalysis is a process that accelerate the rate of chemical reactions with the assistance of catalyst. By offering alternative and energetically favorable mechanisms for the non-catalytic reactions, catalysts can adjust the temperature and pressure

required for the reactions and, thus, enable the reactions to proceed under more accessible conditions.[13 (p.1-22)] Catalysts can be divided into three main categories, which are heterogeneous catalyst, homogeneous catalyst, and enzymatic catalyst. Among them, heterogeneous catalysts are the most widely used and solid catalysts are used in about 90 percent of chemical processes.[14]

Catalysts facilitate reactions by providing active sites that promote the bond breaking reactants and make new bonds while forming the products. For heterogeneous catalysts, the active sites are usually at the surface of a solid and it is desirable to maximize the number of active sites per reactor volume by increasing the specific surface area of the catalyst. Therefore, in general, a heterogeneous catalyst is composed of active substance, a support with a high-surface area, stabilizer and other additives. With different phases, heterogeneous catalysts also have the advantage of being easily separated from the reactants and products. On the contrary, in homogeneous catalysis, the catalysts and reactants are both in the gas phase or in the liquid phase. Because of the full contact with the reactants, homogeneous catalyst exhibits high catalytic efficiency. Moveover, its uniform active site results in high selectivity. According to these strengths, homogeneous catalysts are used extensively in chemical and pharmaceutical production, despite the difficulty to separate catalysts and products.

In recent years, single-atom catalysts and metal-exchange zeolite catalysts have been the subject to interest and research. By dispersing metals into atoms or forming homogeneous complexes, catalysts can have the properties similar to homogeneous catalysts while maintained in the solid phase.[15;16] By linking homo- and heterogeneous catalysis, it is anticipated that the selectivity and activity of heterogeneous catalysts can be improved.

1.2 Ammonia assisted selective catalytic reduction

Nitrogen oxide (NO_x), is an undesirable byproduct during fuel combustion as it contribute to the formation of smog and acid rain.[17;18] In the field of NO_x abatement, NH_3-SCR is the leading technology thanks to efficiency, selectivity and economy.[17] Depending on the NO/NO_x ratio, the reaction is typically considered to occur via the schemes for standard-, fast-, or NO_2-SCR.[12;19;20]

As NO_x emissions from diesel engines are dominated by NO and contain only a small amount of NO_2,[21] standard-SCR reaction that only involve NO, NH_3 and O_2 is considered to be the primary reaction path in the application:

$$4\,NH_3 + 4\,NO + O_2 \rightarrow 4\,N_2 + 6\,H_2O \tag{1.1}$$

When the content of NO_2 increases until the ratio of NO and NO_2 approaches 1:1, the reaction can occur following the fast-SCR scheme:

$$2\,NH_3 + NO + NO_2 \rightarrow 2\,N_2 + 3\,H_2O \tag{1.2}$$

In the cases where the amount of NO_2 is more than twice of NO, the NO_2-SCR reaction that only requires NO_2 and NH_3 will be active:

$$8\,NH_3 + 6\,NO_2 \rightarrow 7\,N_2 + 12\,H_2O \tag{1.3}$$

The sketched reactions are the ideal overall NH_3-SCR reactions as they consume NO_x and fully convert them into N_2 and H_2O. However, depending on the reaction conditions, a variety of side reactions can occur and produce undesirable byproducts. To fulfil the demand of the applications and to restrain the reaction to the preferred direction, improvement of catalyst materials is important.

1.3 Catalysts for NH_3-SCR

In NH_3-SCR, the ideal catalyst should have excellent activity at the conditions of application, be resistance to hydrothermal aging and have a high selectivity toward N_2. It is important to note that the catalyst employed should have weak or even no activity for NO oxidation as NO_2 also is needed to be reduced.

According to the high thermal mass, the temperature before the SCR catalyst could be up to 300 °C.[12] However, in order to achieve better performance and be applicable at different conditions, it is still desirable to achieve high activity also at low temperatures. Presently, vanadia-based catalysts and Fe/Cu-exchanged zeolite catalysts are the main types of catalysts that are utilized for NH_3-SCR thanks to their favorable performance.

1.3.1 Vanadia-based catalysts

Vanadia-based catalysts is one of the common and early commercial catalysts for NH_3-SCR. Generally, vanadia-based catalysts contain 1∼3 % of V_2O_5 as the active component dispersed on a TiO_2 support. 10 % of WO_3 is typically added as a promoter.[12;22] Compared with metal-exchanged zeolite, which is the other common SCR catalyst, vanadium-based catalyst has a stronger resistant to sulfur poisoning.[23] However, it shows a relatively poor low-temperature performance and a weak high-temperature durability. However, a small amount of vanadium can be emitted from the catalyst during high temperature operations, for example during the combustion of coal and heavy fuel oil in industrial combustors.[24] The emitted vanadium compounds, especially vanadium pentoxide (V_2O_5), are considered to be potentially hazardous or carcinogenic and should thus, be control.[24]

1.3.2 Fe/Cu-exchanged zeolite catalysts

As mentioned above, metal-exchanged (mostly Cu and Fe) zeolites have been found to be good catalysts in NH_3-SCR applications and their performance have markedly improved during the last decades.[12] The main advantages of metal-exchange zeolites are that they have a greater hydrothermal stability than vanadia-based catalysts and show a high NO_x conversion over a wide operating temperature range.[12;20;25]

Zeolites are crystalline porous aluminosilicates that exist naturally and can be synthesized.[26] In Fig. 1.1 the structure of SSZ-13 is shown as an example. Owning to the negatively charged oxide frameworks of aluminosilicates, extra positive ions are required to balance the charge and thus make zeolites have the ability to exchange ions such as Na^+, K^+, Cu^+, and Fe^{2+}. As a result, zeolites can provide a ligand system for the exchanged metals and, thus, creating active sites for different reactions.[27]

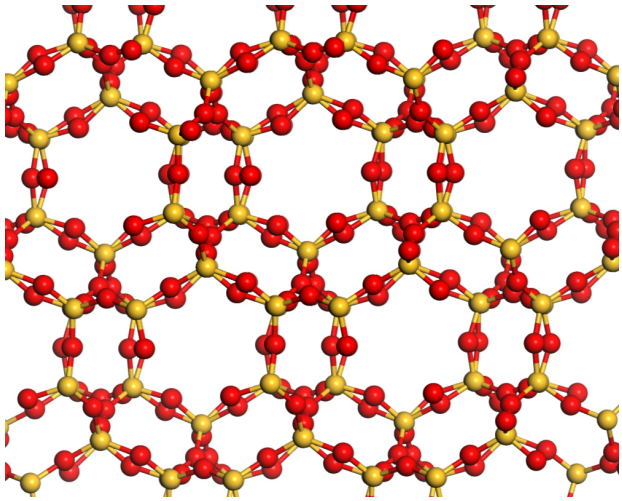

Figure 1.1: Framework structure of SSZ-13.

The pore size of the zeolites has been found to have a significant effect on the catalytic performance, thus, different types of zeolites with varying pore size, such as MOR, FER, BEA, ZSM-5 and SSZ-13 have been studied.[28;29] It has been shown that zeolites with small pore sizes give a better activity and selectivity for NH_3-SCR.[30;31] When comparing the hydrothermal stability, low-temperature activity and N_2 selectivity of NH_3-SCR, Cu-SSZ-13 with a chabazite structure (hereinafter referred to as Cu-CHA) is generally superior to other catalysts.[12;29;31;32] According to its excellent NO_x reduction activity, Cu-CHA has been brought into commercial applications.[20;31] However, despite its good catalytic properties, further research and improvement over Cu-CHA is necessary to meet the increasingly stringent emission standards worldwide.

The detailed catalytic mechanisms of NH_3-SCR over Cu-CHA have been studied and debated over the past years. At present, based on in situ X-ray absorption spectroscopy experiments and density functional theory calculations, it is general accepted that NH_3-SCR reaction proceeds via redox steps over mobile Cu species.[33] During this reaction, the Cu ions are reduced from Cu(II) to Cu(I) and oxidized back to Cu(II) in the oxidation step. The intermediates HONO and H_2NNO are formed over the Cu site and decomposed over the Brønsted acid site.[34] With the joint action of mobile Cu species and Brønsted acid site, Cu-CHA gives a high activity of low-temperature NH_3-SCR.

Noteworthy, a recent analogous study[35] suggested that NH_3SCR over Vanadia-based and Cu-zeolite catalysts follow a similar general mechanism based on reduction/oxidation half-cycles, which gives novel insights into the catalytic mechanism study.

1.4 N_2O formation

The aim of introducing NH_3-SCR catalysts in the aftertreatment system is to convert the NO_x in exhaust gases into harmless N_2 and H_2O. However, as the selectivity to N_2 during the reaction is not complete, a small amount of by-products are generated. Among

the byproducts, the most undesired one is nitrous oxide (N_2O), which contributes to the greenhouse effect and ozone layer depletion.[36] According to its powerful greenhouse effect, the emission of N_2O needs to be reduced.

There are different perspectives on the exact mechanism of N_2O formation during NH_3-SCR, but it is generally agreed that the reaction follows some of the general reaction schemes below:[37;38]

$$4\,NH_3 + 4\,NO + 3\,O_2 \rightarrow 4\,N_2O + 6\,H_2O \tag{1.4}$$

$$4\,NH_3 + 4\,NO_2 + O_2 \rightarrow 4\,N_2O + 6\,H_2O \tag{1.5}$$

$$6\,NH_3 + 8\,NO_2 \rightarrow 7\,N_2O + 9\,H_2O \tag{1.6}$$

$$2\,NH_3 + 4\,NO \rightarrow 2\,N_2 + N_2O + 3\,H_2O \tag{1.7}$$

It is currently assumed that under NH_3-SCR reaction conditions, NH_3 can react with the surface nitrates forming ammonium nitrate (NH_4NO_3) over the catalysts.[39] NH_4NO_3 can further decompose into N_2O and H_2O, which is the proposed source of N_2O.[39;40]

$$NH_4NO_3 \rightarrow N_2O + 2\,H_2O \tag{1.8}$$

In the NH_3-SCR over Cu-CHA with low Cu-loading, N_2O is mainly released above 250 °C, which is slightly lower than the formation of N_2O from the gas phase thermal decomposition of NH_4NO_3 (>290 °C).[41;42] However, for cases with higher Cu-loading, the N_2O emission peak shifts to lower temperatures (about 200 °C) that is significantly lower than the thermal decomposition of NH_4NO_3. Hence, there is a reason to suggest that when a sufficient amount of copper is present in the catalyst, N_2O can be generated via a low-energy barrier pathway.

In addition to the Cu loading, the NO_2/NO_x ratio is also a factor that affects the selectivity in NH_3-SCR. The onset temperature for N_2O does not depend sensitively on the NO_2/NO_x ratio, however the yield of N_2O increases with the NO_2/NO_x ratio.[38;43]

1.5 Objectives

The objective of this work is explore the catalytic mechanism of N_2O formation during NH_3-SCR over Cu-CHA and provide strategies to enhance the selectivity to N_2 during NH_3-SCR.

In **Paper I**, the formation of N_2O over gas-phase, Al-free CHA and H-CHA from NH_4NO_3 decomposition was explored. The comparison between Al-free and H-CHA show that Brønsted acid site can promote the decomposition process. More importantly, a novel path for N_2O formation via H_2NNO decomposition was suggested. This path is based on the previously proposed multisite reaction mechanism which considered the acitve site of NH_3-SCR is the Cu-peroxo complex.[34]

In **Paper II**, a first principles microkinetic model was constructed to investigate low-temperature NH_3-SCR over Cu-CHA. This model is based on the proposed multisite reaction and further improved by the alternative steps as well as the N_2O formation path in **Paper I**. The calculated values for activation energy and reaction orders based on the model show a good agreement with the experimental data. Moreover, a degree of rate

control analysis reveals how the rate-controlling step change with temperatures and gives unique insights in the function od Cu-CHA catalysts for NH_3-SCR.

The work gives a good example that it is possible to connect experimental and theoretical catalysis in a direct manner. With this approach, it has been possible to clarify the complex catalytic processes of NH_3-SCR and provide theoretical guidance to promote the catalytic performance of Cu-CHA. Moreover, one of the main goals of current work is to contribute to the development of exhaust gas aftertreatment systems that can meet the stringent emission standards.

Chapter 2

Electronic structure calculations

'The underlying physical laws necessary for the mathematical theory of a large part of physics and the whole of chemistry are thus completely known, and the difficulty is only that the exact application of these laws leads to equations much too complicated to be soluble. It therefore becomes desirable that approximate practical methods of applying quantum mechanics should be developed, which can lead to an explanation of the main features of complex atomic systems without too much computation.' Paul Dirac (1929)[44].

The electronic energy and, thus, the calculation of electronic structure is the starting point for first principles simulations of chemical transformations. The Schrödinger equation is the cornerstone, and how to solve this many-body equation in a proper way is a long-standing challenge. Approximations have evolved over the years and Hartree-Fock theory as well as density functional theory (DFT) are the two main approaches to obtain the electronic energy. The calculations in this thesis are performed using the DFT, and the foundation as well as developments of DFT will be presented in this chapter.

2.1 The Schrödinger equation

The total energy of a set of electrons and nuclei is within quantum mechanics described by the Schrödinger equation:

$$\hat{H}\Psi = E\Psi \tag{2.1}$$

Where $\hat{H}$ is the Hamiltonian operator corresponding to the total energy of the system and Ψ is the wave function. In the absence of magnetic or electric fields, the $\hat{H}$ for a many-body system of n nuclei and e electrons is given by (in atomic Hartree units):

$$\begin{aligned}\hat{H} = &\sum_{\alpha=1}^{n}\left[-\frac{\nabla_{R_\alpha}^2}{2n_\alpha} + \frac{1}{2}\sum_{\beta=1}^{n}\frac{Z_\alpha Z_\beta}{|R_\alpha - R_\beta|}\right] + \sum_{i=1}^{e}\left[-\frac{\nabla_{r_i}^2}{2} + \frac{1}{2}\sum_{j=1}^{e}\frac{1}{|r_i - r_j|}\right] \\ &- \frac{1}{2}\sum_{i=1}^{e}\sum_{\alpha=1}^{n}\frac{Z_\alpha}{|r_i - R_\alpha|}\end{aligned} \tag{2.2}$$

Here the first term is the nuclei kinetic energy and nuclei-nuclei interaction, the second term is the electron kinetic energy and electron-electron interaction, and the last term is the nuclei-electron interaction. Thus, the many-body Hamiltonian can be written as:

$$\hat{H} = \hat{H}_{nn} + \hat{H}_{ee} + \hat{H}_{ne} \tag{2.3}$$

2.2 The Born-Oppenheimer approximation

Although the Schrödinger equation describes the many-body system. It can only be solved analytically for one-electron systems. In order to simplify the many-body problem, the Born-Oppenheimer approximation [45] is generally the first step. The approximation separates the electronic and nuclear wavefunctions and is based on the large difference in the speeds of electrons and nuclei. As electrons move much faster than the nuclei, it is possible to treat the electrons as moving in the electrostatic field created by the nuclei. Following the Born-Oppenheimer approximation, the many-body Hamiltonian $\hat{H}$ can be represented by the electronic Hamiltonian $\hat{H}_e$ and nuclei Hamiltonian $\hat{H}_n$. The electronic Hamiltonian $\hat{H}_e$ is:

$$\hat{H}_e = \hat{T} + \hat{V}_{ext} + \hat{V}_{ee} \tag{2.4}$$

Where $\hat{T}$ is the kinetic energy operator for the electrons, $\hat{V}_{ext}$ is the external potential of the nuclei field, and $\hat{V}_{ee}$ is the electron-electron interactions. Although the Born-Oppenheimer approximation simplifies the Schrödinger equation, it can not be solved exactly for systems with many electrons.

2.3 The density functional theory

To bring Schrödinger equation into practical use, different methods have been developed to actually solve the many-electrons problem. One of the most widely used approaches today is DFT, which is based on the Hohenberg-Kohn theorems, [46] which states that the ground-state density $n_0(r)$ is a unique functional of the external potential $\hat{V}_{ext}$ and the ground-state energy can be determined by $\hat{V}_{ext}$. In this way, the energy and the intricate many-body effects of the system can be described by the electron density. [47]

2.3.1 The Kohn-Sham formulation

Although the Hohenberg-Kohn theorem connects the electron density and the energy of the system by an energy functional, the form of the functional is still unknown. With the introduction of one electron orbitals, the Kohn-Sham formalism was developed, which provides a possibility to treat many electrons systems with a reasonable accurately. [48;49] The ground state energy is within the Kohn-Sham written as

$$E[n] = T_s[n] + J[n] + V_{ext}[n] + E_{xc}[n] \tag{2.5}$$

The first term is the kinetic energy for a noninteracting reference system, the second term is the classical electron-electron repulsion energy and the third term is the nuclei-electron potential energy. These three terms can be calculated to obtain an exact solution. However, the fourth term, which is the exchange-correlation energy ($E_{xc}[n]$) has no explicit form and will be discussed further in the next subsection.

With the explicit form of the first three term, the ground state electronic energy of a system can be written as

$$E[n] = \sum_i \langle \phi_i | -\frac{1}{2}\nabla^2 | \phi_i \rangle + \frac{1}{2}\iint \frac{\rho(r)\,\rho(r')}{|r-r'|} dr\, dr' + \int \rho(r)\, v(r) dr + E_{xc}[n] \tag{2.6}$$

Here ϕ_i is the set of one-electron KS orbitals and $\rho(r)$ is the electron density of the KS reference system, which is given by

$$\rho(r) = \sum_i |\phi_i(r)|^2 \tag{2.7}$$

In the nuclei-electron potential energy term, $v(r)$ is the external potential related to the nuclei and can be represented by

$$v(r) = -\sum\nolimits_A \left(\frac{Z_A}{|\mathrm{r} - \mathrm{R}_A|} \right) \tag{2.8}$$

Where Z_A is the charge of the nuclei, and $|\mathrm{r} - \mathrm{R}_A|$ is the distance between the nuclei and the electron.

2.3.2 Approximations to the exchange-correlation functional

The exchange-correlation functional, which is the $E_{xc}[n]$ term in the Kohn-Sham formulation is associated with the quantum mechanical effects of the electron-electron interactions.[49] $E_{xc}[n]$ can be regarded as the sum of an exchange term $E_x[n]$ and a correlation term $E_c[n]$. The description of the $E_{xc}[n]$ term is the biggest challenge of DFT and the approximate nature of the exchange-correlation functional limits the accuracy of the method.

Various approximations have been developed with the attempt to reach the "heaven" of chemical accuracy, which is the famous Jacob's ladder of approximations toward the unknown exact exchange-correlation functional.[49] Some common approximations are discussed below.

Local density approximation

The local density approximation is the simplest approach to describe the exchange functional. It used the expression of the uniform electron gas model[46] to represent the exchange energy of the electron density of the studied system. The early expression of the exchange energy is given by Dirac in 1930[50]

$$E_x^{\mathrm{LDA,Dirac}}[n] = -\frac{3}{4}\left(\frac{3}{\pi}\right)^{\frac{1}{3}} \int \rho^{\frac{4}{3}} dr \tag{2.9}$$

The correlation energy $E_c[n]$ can for the uniform electron gas be obtained by exact quantum Monte Carlo simulation.[51] Such simulations have been parametrization to develop correlation functionals.[52]

Although the concept of LDA is relatively simple, this approximation is surprisingly accurate especially for the simple metal systems that have close to homogeneous valence electron densities. However, there are still some deficiencies, such as the incomplete elimination of self-interaction.[49] In applications, LDA gives reasonable geometries but normally overestimate the ionization energies and bond strengths.[47;49] As LDA is based on the uniform electron gas model, systems with large gradients in the valence electron density will not be accurately described.

Generalized gradient approximation

To obtain an accurate description for molecular systems that have an inhomogeneous electron density, better methods that not only depend on the density but also gradient of the density ($\Delta\rho(r)$) have been developed.[53] In the early work, the gradient expansion approximation (GEA) was introduced to provide a gradient correction to the standard exchange energy density in a situation with slowly varying density.[54] The gradient expansion is developed by the dimensionless reduced gradient, which is given by

$$x = \frac{|\nabla\rho|^{\frac{4}{3}}}{\rho} \tag{2.10}$$

and the exchange energy from gradient expansion approximation can be represented as

$$E_x^{\mathrm{GEA}} = -\int \rho^{\frac{4}{3}} \left[\frac{3}{4}\left(\frac{3}{\pi}\right)^{\frac{1}{3}} + \frac{7}{432\pi(3\pi^2)^{\frac{1}{3}}}x^2 + ...\right] dr \tag{2.11}$$

However, GEA can apply only for the systems that have slowly varying electron densities. For systems that have exponentially decaying density ($x \to \infty$), GEA will not be able to give a accurate result.[47] The development of generalized gradient approximation (GGA) reduces the problem by introducing the gradient expansion in the low x limit (represented as $F(x)$), where the energy is given by:[47]

$$E_x^{\mathrm{GGA}}[n, x] = \int \rho^{\frac{4}{3}} F(x) dr \tag{2.12}$$

There are many gradient correlated exchange functionals including B88, PW, and PBE that are based on the GGA, which enhances the accuracy of the exchange-correlation energy. In recent years, meta-GGA methods that take additional semi-local information into account have been proposed and have shown to provide higher accuracy.[55] In this thesis, I have adopted the GGA functional PBE.[53]

Hybrid GGA

One of the main source of the inaccuracy in DFT is the self-interaction error (SIE), which comes from the fact that the electron-electron interaction in the classical Coulomb energy, is not cancelled the corresponding interaction in the exchange part.[56;57] However, in the wavefunction-based Hartree-Fock theory, the self-interaction is cancelled exactly. According to this property, hybrid functionals which are the combination of the exchange-correlation functional from GGA method and a certain amount of Hartree-Fock (HF) exchange were developed.[47;57] With the successful cancellation of the SIE, hybrid functionals reach higher level of accuracy.

Through the combination between several functionals and fitting parameters through experiments, a new functionals called B3LYP[58] was proposed:

$$E_{xc}^{\mathrm{B3LYP}} = 0.2\, E_x^{\mathrm{HF}} + 0.8\, E_x^{\mathrm{LDA}} + 0.72\, \Delta E_x^{\mathrm{B88}} + 0.81\, E_c^{\mathrm{LYP}} + 0.19\, E_c^{\mathrm{VWN}} \tag{2.13}$$

Although hybrid GGA can achieve high accuracy, it is still not a universal functional. For the systems with homogeneous electron gas, the atomization energies from B3LYP are inaccurate.[59]

In addition to B3LYP, the Heyd-Scuseria-Ernzerhof hybrid functional (HSE)[60] is another promising hybrid functional. In HSE, spatial decay of the HF exchange interaction is accelerated by substitution of the full $1/r$ Coulomb potential with a screened one. In this way, the computational cost for calculations in extended systems can be reduced significantly and it also gives good accuracy for lattice constants and band gaps in oxides.

DFT+U

As mentioned, conventional LDA and GGA methods have difficulties to accurately describe strongly correlated materials due to the pronounced trend to delocalize electrons in LDA and GGA.[61] To describe these correlated systems where electron should be localized accurately, a Hubbard term have been introduced based on the assumption that the strongly correlated d or f electrons are governed by on-site quasiatomic interactions.[62] The definition of Hubbard parameter U is

$$U = E(d^{n+1}) + E(d^{n-1}) - 2E(d^n) \tag{2.14}$$

which measures the cost of Coulomb-energy for putting two electrons at the same site. In this way, the self-interaction error can be partly eliminated and thus, make the DFT+U method have better accuracy of correlated systems. In my work, it was been important to use DFT+U to correctly describe the localize Cu(3d) electrons.

Van der Waals interaction

For unbound chemical species, long-range electronic correlations exist between the non-overlapping densities and these correlations are the so-called van der Waals (vdW) interactions. However, the vdW interactions are not included in pure DFT-based functionals[47] and leads to an inaccuracy in the description of sparse matter.

The vdW-DF functional proposed by Lundqvist et al,[63] take the long-range interactions in to account by adding a long-range form of the interactions.

An alternative semi-empirical approach, is to introduce the correct attractive $1/R^6$ behavior by adding the empirical pairwise corrections. These functionals are called DFT-D and DFT-D3[64] is employed in this work.

2.3.3 Solution to the Kohn-Sham equations

DFT is used in electronic structure calculations to simplify the many-body Schrödinger equation to one-particle Kohn-Sham equations. To bring DFT into practice, different approaches have been adopted to solve the Kohn-Sham equations. One important choice is the method of expanding the wavefunctions. In this work, the studied system have periodic boundary condition, thus, plane waves that have inherent periodicity is chosen to expand the Kohn-Sham orbitals. Besides the way to expand the wavefunctions, one needs to consider how to treat the core electrons. One of the most widely used methods

is the projector augmented-wave (PAW) method proposed by Blöchl in 1994.[65] In the PAW method, the all-electron (AE) wavefunctions is transformed into computationally convenient pseudo (PS) wavefunctions. Here the AE wavefunctions is a full one-electron Kohn-Sham wavefunction while the PS wavefunctions is set to be the wavefunctions of the pseudopotential approach or the envelope functionals of the linear methods. Through the transformation, AE wavefunction can be describe by the equation below that from the PS wavefunction:

$$|\Psi\rangle = |\tilde{\Psi}\rangle + \sum_i (|\phi_i\rangle - |\tilde{\phi}_i\rangle)\langle\tilde{p}_i|\tilde{\Psi}\rangle \tag{2.15}$$

Here $|\phi_i\rangle$ is the AE partial waves, $|\tilde{\phi}_i\rangle$ is one PS partialwave, and $|\tilde{p}_i\rangle$ is the projector functional for each PS partial wave that localized with the augmentation region. In this thesis, Vienna ab initio simulation package (VASP)[66;67] is employed to do the calculations.

To obtain the ground state solution from the Kohn-Sham equations, a self-consistent field (SCF) loop is applied in the calculations. A schematic is shown in Fig. 2.1. The loop starts with an initial guess of the plane-wave weights and electron density. The Kohn-Sham equation are solved by calculating the effective potential. A new electron density and effective potential will be obtained. Every time after solving the equation, the energy different between the latest effective potential ($v_{eff,j+1}$) and effective potential from previous loop ($v_{eff,j}$) will be compared until the latest solution reaches the criteria of convergence.

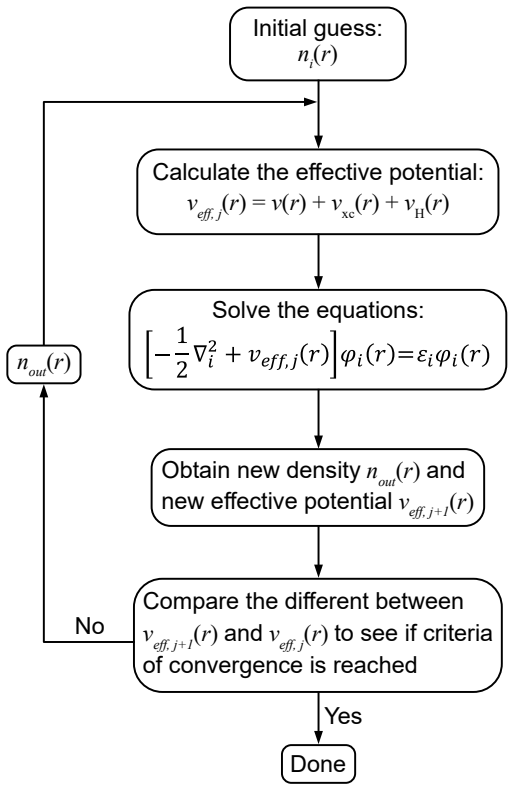

Figure 2.1: Schematic of self-consistent field (SCF) loop to obtain the ground state. Adapted from Ref. 68.

Chapter 3

Calculations of measurable properties

The previous chapter introduced the approximations and methods connected to DFT, which is how I calculated the total electronic energy. The development of DFT has greatly advanced the practical use of theoretical calculations in materials science. With DFT it is possible to calculate and predict geometrical structures, various physical properties and reaction processes that involve electronic hybridizations. Calculations of measurable properties is discussed in this chapter.

3.1 Geometry optimization

In the electronic structure calculation, the structure of investigated system is specified by the atom type and position of the atoms that compose the system. For an arbitrary structure, the electronic structure can be calculated and the corresponding total energy can be obtained. By comparing the energy of the same system with different atomic arrangements, it is possible to find the structure that has the lowest energy. The structure with the lowest energy is the most stable structure and also the most probable structure. The operation of finding the most stable structure is the, so-called, geometry optimization. Various methods exist to optimize the structure in a proper way.[69]

By use of a local quadratic approximation, the first and second derivatives of the energy for the geometrical parameters construct the potential energy surface via

$$E(\mathrm{x}) = E(\mathrm{x}_0) + \mathrm{g}_0^T \Delta\mathrm{x} + \frac{1}{2}\Delta\mathrm{x}^T \mathrm{H}_0 \Delta\mathrm{x} \tag{3.1}$$

Here gradient ($\mathrm{d}E/\mathrm{dx}$) at x_0 is represented by g_0, the Hessian ($\mathrm{d}^2E/\mathrm{dx}^2$) at x_0 is given by the H_0 and $\Delta\mathrm{x} = \mathrm{x}\text{-}\mathrm{x}_0$. By probing the potential energy surface, it is possible to obtain a minimum energy as well as the corresponding structure. The techniques used for geometry optimization are presently mainly depended on the first derivative of the energy. The current major methods are the Newton and quasi-Newton methods, and the conjugate gradient methods, such as GDIIS. In VASP, the conjugate-gradient method was implemented to find the optimized structure and minimum total energy.

In my work, which is focus on the reactions over Cu-CHA, it is difficult to search for a local minimum due to the flat potential energy surface. To obtain the low-energy configurations, *ab initio* molecular dynamics simulation was adopted as an additional tool, which will be introduced in the next section.

3.2 Ab initio molecular dynamics

The motion of molecules under different conditions or environments is a matter of great interest in theoretical calculations. The concept of *ab initio* molecular dynamics (MD)[70] is that the motion of the atoms can be calculated by solving the Newtons laws of motion ($F = ma$) with a force obtained by DFT. By the Verlet algorithm, the equation of motion is integrated via:[70]

$$r_i(t + \Delta t) \cong 2r_i(t) - r_i(t - \Delta t) + \frac{F_i(t)}{m_i}\Delta t^2 \tag{3.2}$$

Besides of predicting the motion, MD calculations can be used to search for low-energy configurations for systems with a flat potential energy surface. In this thesis, Born-Oppenheimer MD (BOMD) was performed in the canonical (NVT) ensemble to obtain the low-energy configurations.

3.3 Vibrational frequency analysis

Vibrational spectroscopy is of great importance in chemical research because it provides fingerprints of molecules. Based on the vibrational modes, the composition and structure of molecules can be determined. By the comparison of computed and observed frequencies, many molecules have been identified.[71 (p. 130)] Moreover, the calculated frequencies are also used to calculate the zero point energy, the vibrational entropy and to characterize minimum and saddle points on the potential energy surface.

The vibrations of a molecule can be seen as displacements of the atoms from the equilibrium structure. It is possible to expand the energy of the molecule around the equilibrium bond length by a Taylor expansion. The harmonic approximation neglects the higher order terms in the Taylor expansion and the vibrational frequency can be obtained by combining Newton's and Hooke's laws.[72] For a system that have N atoms, there will be $3N$ degree of freedom and the Taylor expansion of the energy for the atoms in the local minimum r_0 can be expressed as:

$$E = E_0 + \frac{1}{2}\sum_{i=1}^{3N}\sum_{j=1}^{3N}\left[\frac{\partial^2 E}{\partial_{\mathrm{x}i}\partial_{\mathrm{x}j}}\right]_{\mathrm{x}=0}\Delta\mathrm{x}_i\Delta\mathrm{x}_j \tag{3.3}$$

where $\Delta\mathrm{x}_i$ is the displacement and a $3N \times 3N$ matrix which is the so-called Hessian matrix, is defined by the derivatives. Following that, the normal modes are given by the $3N$ eigenvalues of the matrix. It should be noted that non-linear molecules have $3N$-6 vibrations while linear molecules have $3N$-5 vibrations. The removed frequencies included 3 translations and 3 (or 2) rotations.

3.4 Transition state and energy barriers

Based on the experimental observations, Arrhenius proposed an empirical expression for the rate constant of a reaction. The Arrhenius equation is given by:

$$k = \mathrm{A}e^{-\frac{E_a}{k_\mathrm{B}T}} \tag{3.4}$$

Here A is the pre-exponential factor, k is the reaction rate constant at the absolute temperature (T), k_{B} is Boltzmann's constant, and E_a is the activation energy.

The concept of activation energy is highlighted in the Arrhenius equation and arisen also in transition state theory (TST).[13 (p. 107-109)] In TST, it is assumed that the reactants (R) are activated to the transition state ($\mathrm{R}^{\#}$) in order to form the product (P).[13 (p. 108)] $\mathrm{R}^{\#}$ is the configuration that have the highest energy along the reaction coordinate. The schematic of transition state is shown in Fig. 3.1. The energy difference (ΔE) between $\mathrm{R}^{\#}$ and R is the activation energy of the reaction.

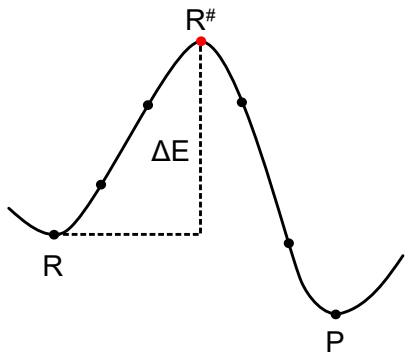

Figure 3.1: Schematic of the transition state theory (TST).

Following the assumptions, a reaction can be described by reaction coordinate, which is usually a vibration. The rate of a reaction to reach the transition and end up at the product can be evaluated by the frequency of the reaction coordinate. The expression of rate constant within TST is:

$$k^{\mathrm{TST}} = \frac{k_{\mathrm{B}}T}{h}\frac{Z^{\ddagger}}{Z} \tag{3.5}$$

Here T is temperature, and h is Planck's constant. Z and $Z^{\ddagger}$ are the partition functions of the initial state and the transition state without the reaction coordinate, respectively. In TST, the initial and transition states are assumed to be in equilibrium, which leads to the following expression for the rate constant:[73 (p. 109)]

$$k^{\mathrm{TST}} = \frac{k_{\mathrm{B}}T}{h}e^{-\Delta G^{\ddagger}/k_{\mathrm{B}}T} = \frac{k_{\mathrm{B}}T}{h}e^{\Delta S^{\ddagger}/k_{\mathrm{B}}}e^{-\Delta H^{\ddagger}/k_{\mathrm{B}}T} \approx \frac{k_{\mathrm{B}}T}{h}e^{\Delta S^{\ddagger}/k_{\mathrm{B}}}e^{-\Delta E^{\ddagger}/k_{\mathrm{B}}T} \tag{3.6}$$

Where $\Delta G^{\ddagger}$ is the difference in Gibbs free energy between the initial and transition states. $\Delta S^{\ddagger}$ and $\Delta H^{\ddagger}$ are the corresponding differences in entropy and enthalpy, respectively. The pV-dependence in the enthalpy is neglected so the change enthalpy becomes equal to the change in energy ($\Delta E^{\ddagger}$).

By evaluating the reaction rate and derive other experimentally measurable kinetic parameters, theoretical calculations can be connected and compared with experimental measurements.

3.4.1 Transition state search

In a transition state search, the minimum energy path between the initial and final state is probed. The top of the minimum energy path is the transition state, which is also the saddle point of the potential surface. It should be noted that the saddle point is the local maxima along the reaction direction but the local minimum in all other directions. To find the minimum energy path, different methods have been developed and the nudged elastic band (NEB) method is an efficient method that being widely used.[74]

The NEB method works by constructing a number of images between the initial and final state. Spring forces are added along the band between images to ensure the continuity of the path and that is also why the method is called elastic band. When finding the lowest energy possible of each image, the tangent to the path will be estimated at every iteration in order to decompose the true force and the spring force. Only the perpendicular component of the true force and the parallel component of the spring force are included during the minimization[74]

3.5 Bader charge analysis

Bader charge analysis[75] is a useful method to evaluate the distribution of the electron density, which can also provide information on change transfer. The principle of charge analysis is to split the characteristic of the molecule into contributions from each atom. Bader suggested that the space in the systems can be divide by the charge density and the divided space is called Bader volumes. The difficulty of Bader analysis is the calculation of Bader volumes. The grid-based Bader algorithm used in this thesis allows convergence in the limit of fine charge density lattices and thus, suitable for large DFT calculations.[76]

Chapter 4

Evaluation of entropy

From eq. (3.6), it can be inferred that accurate estimations of entropy and enthalpy changes are important to obtain rate constants that reflect the actual reaction. As the NH_3-SCR reaction is carried out in Cu-CHA, the system is more complex than typical surface reactions. There are two main types of adsorption sites of NH_3 in Cu-CHA, namely the Brønsted acid site and the Cu-site. When NH_3 is adsorbed on the Brønsted acid site, it will exist in the form of NH_4^+. For the adsorption on the Cu-site, up to four NH_3 can bind to one Cu at the same time and form $[Cu(NH_3)_n]^+$ (n = 1 - 4). Without NH_3 adsorption, the Cu cation is initially located in the centre of the six-membered ring in the CHA. When the first NH_3 is adsorbed on Cu^+, the Cu cation is pulled up but still bonded to the CHA framework. Once $[Cu(NH_3)_{n\geq 2}]^+$ is formed, the complex will leave the framework and become a mobile species. The optimized structures of NH_4^+ in H-CHA, framework-Cu, and $[Cu(NH_3)_n]^+$ (n = 1 - 4) from DFT calculation are shown in Fig. 4.1. The mobility of NH_3-solvated Cu-complexes has been verified by X-ray absorption spectroscopy measurements.[77;78]

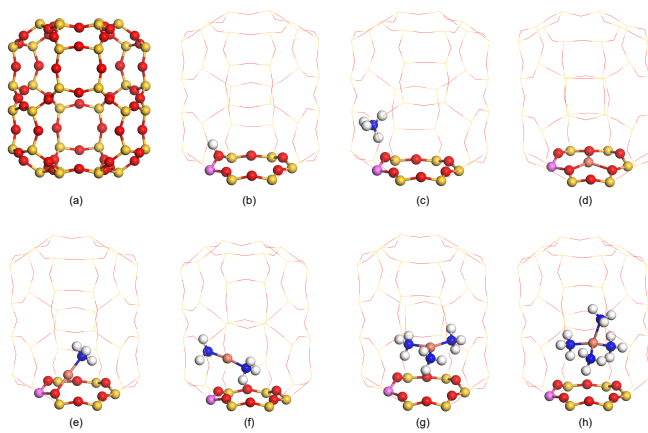

Figure 4.1: Structures of CHA models. (a) Al-free CHA, (b) H-CHA, (c) NH_3 on Brønsted acid site (forming NH_4^+) (d) Cu cation on Al-CHA, and (e - h) $[Cu(NH_3)_n]^+$ (n = 1 - 4) in CHA. Atomic color codes: H (white), N (blue), O (red), Si (yellow), Al (pink) and Cu (bronze).

This chapter elaborates on the method used in the entropy evaluations and shows the validation that has been done by comparisons to NH_3-temperature programmed desorption (NH_3-TPD) experiments.

4.1 Entropy evaluation in different cases

Based on statistical mechanics and thermodynamics,[79] the entropy (S) is calculated from the partition function (Z):

$$S = -\frac{\partial}{\partial T}(-k_{\mathrm{B}}T\ln Z)_{V,N} = k_{\mathrm{B}}\ln Z + k_{\mathrm{B}}T\frac{1}{Z}\left(\frac{\partial Z}{\partial T}\right)_{V,N} \tag{4.1}$$

Z is the product of the contributions from translations, rotations, and vibrations. The entropy depends mainly on translations and the partition function of translations can be significantly influenced by restricting this degree of freedom. In order to have a accurate evaluation of the entropy of different Cu complexes in Cu-CHA, different methods have been adopted.

4.1.1 Entropy for gas-phase molecules

A gas-phase molecule is a free translator in a confined three-dimensions space. The volume of this space is given by the pressure through the ideal gas law for one molecule ($pV = k_{\mathrm{B}}T$). In this case, the total partition function and the total entropy is[73 (p. 87-91)]:

$$Z^{\mathrm{gas}} = Z^{\mathrm{gas}}_{\mathrm{rot}} Z^{\mathrm{gas}}_{\mathrm{vib}} Z^{\mathrm{gas}}_{\mathrm{trans}} \tag{4.2}$$

$$S^{\mathrm{gas}} = S^{\mathrm{gas}}_{\mathrm{vib}} + S^{\mathrm{gas}}_{\mathrm{rot}} + S^{\mathrm{gas}}_{\mathrm{trans}} \tag{4.3}$$

Here, $S^{\mathrm{gas}}_{\mathrm{vib}}$, $S^{\mathrm{gas}}_{\mathrm{rot}}$, and $S^{\mathrm{gas}}_{\mathrm{trans}}$ are the vibrational, rotational, and translational entropies, respectively.

Contributions from translations

The translational partition function for gas-phase molecule is:[73 (p. 86)]

$$Z^{\mathrm{gas}}_{\mathrm{trans}} = (\frac{2\pi m k_B T}{h^2})^{\frac{3}{2}} V \tag{4.4}$$

m is the mass of the molecule and the volume (V) is obtained by the pressure and temperature ($V = k_{\mathrm{B}}T/p$). Following eq. (4.1), the translational entropy per molecule is:[80]

$$S^{\mathrm{gas}}_{\mathrm{tran}} = k_{\mathrm{B}}(\ln(Z^{\mathrm{gas}}_{\mathrm{trans}}e) + T(\frac{3}{2T})) = k_{\mathrm{B}}(\ln Z^{\mathrm{gas}}_{\mathrm{trans}} + \frac{5}{2}) \tag{4.5}$$

Contributions from rotations

The rotational partition function of a molecule depends on the structure and have different expression for linear (4.6) and non-linear (4.7) molecule:

$$Z^{\mathrm{gas}}_{\mathrm{rot_{linear}}} = \frac{1}{\sigma}(\frac{8\pi^2 I k_B T}{h^2}) \tag{4.6}$$

$$Z^{\mathrm{gas}}_{\mathrm{rot_{non-linear}}} = \frac{\sqrt{\pi}}{\sigma}(\frac{8\pi^2 I k_B T}{h^2})^{\frac{3}{2}}\sqrt{I_x I_y I_z} \tag{4.7}$$

Here σ is the symmetry factor of molecule and I_i are the moments of inertia. The I_i values used in this thesis were obtained through the Atomic Simulation Environment (ASE).[81;82] The partial derivative term of Z_{rot} is equal to $3/2T$ for non-linear molecule while it is $1/T$ in linear molecule. Thus, the equation of rotational entropy per molecule can be expressed as:

$$S^{\mathrm{gas}}_{\mathrm{rot_{linear}}} = k_{\mathrm{B}}(\ln Z^{\mathrm{gas}}_{\mathrm{rot_{non-linear}}} + 1) \tag{4.8}$$

$$S^{\mathrm{gas}}_{\mathrm{rot_{non-linear}}} = k_{\mathrm{B}}(\ln Z^{\mathrm{gas}}_{\mathrm{rot_{non-linear}}} + \frac{3}{2}) \tag{4.9}$$

Contributions from vibrations

As mentioned in section 3.3, the number of vibrational frequencies is $3N$-6 for non-linear molecules, while it is $3N$-5 for linear molecules when N is the number of atoms in the molecule. Based on the harmonic approximation,[73 (p. 90)] the vibrational entropy can be described by the vibrational frequencies:

$$\begin{aligned} S^{\mathrm{gas}}_{\mathrm{vib}} &= k_{\mathrm{B}}(\ln(Z^{\mathrm{gas}}_{\mathrm{vib}}e) + T(\frac{\partial \ln Z^{\mathrm{gas}}_{\mathrm{vib}}}{\partial T})_V) \\ &= k_{\mathrm{B}}\sum_m(\frac{\Theta_{v,m}/T}{e^{\Theta_{v,m}/T}-1} - \ln(1-e^{-\Theta_{v,m}/T})) \end{aligned} \tag{4.10}$$

Here the vibrational mode is represented by m. In the zero-point energy calculations, the first vibrational energy have been chosen as the reference point, thus, the equation of vibrational entropy per molecule is expressed as:

$$\begin{aligned} S^{\mathrm{gas}}_{\mathrm{vib}} &= k_{\mathrm{B}}(\ln(Z^{\mathrm{gas}}_{\mathrm{vib}}e) + T(\frac{\partial \ln Z^{\mathrm{gas}}_{\mathrm{vib}}}{\partial T})_V) \\ &= R\sum_m(\frac{1}{(1-e^{-\Theta_{v,m}/T})}) \end{aligned} \tag{4.11}$$

Here Θ is the vibrational temperature, which is defined as:

$$\Theta_{v,m} = \frac{hv}{k_B} \tag{4.12}$$

where v is the vibrational frequency.

4.1.2 Entropy for adsorbates

Depending on the adsorption situation, two different methods have mainly been used to estimate the entropy of adsorbates in CHA. It is generally assumed that when the molecule is pinned by a chemical bond to the surface, it will lose all the rotations and translations. In this way, the entropy of adsorbates on surface can be calculated with the

vibrational modes by the harmonic approximation. However, for $[Cu(NH_3)]^+$, which is bound to CHA framework, due to the single bond between Cu and the framework, Cu still maintains a part of translations and rotations, which make the entire complex more mobile than adsorbates on surface. In this case, the total entropy of $[Cu(NH_3)]^+$ will be underestimated using the harmonic approximation only for the adsorbed NH_3. Therefore, the entropy of $[Cu(NH_3)]^+$ is evaluated as the vibrational entropy of the entire complex which have 5 atoms. In the harmonic approximation, only the last three modes have been removed. Herein, 12 modes of $[Cu(NH_3)]^+$ were used for the entropy calculation.

For the entropy of framework-Cu species, we turned to a more refined approach rather than the harmonic approximation, which is the complete potential energy sampling (CPES) method.[83] In this approach, the translational partition function is estimated by explicit calculations of the potential energy of the adsorbates. This semiclassical canonical partition function is given by:

$$Z_{\text{trans}}^{\text{CPES}} = \frac{2\pi m k_{\text{B}} T}{h^2} \iint exp\left(\frac{-V(x,y)}{k_{\text{B}} T}\right) dx\, dy \tag{4.13}$$

Where the integration is performed numerically over the surface cell, and $V(x, y)$ is the potential energy as a function of position (x, y) as obtained by first principles calculations. The potential energy $V(x, y)$ is obtained in practice by interpolation between a set of calculated points in the surface cell. In this thesis, the complete potential energy sampling of Cu cation adsorbed on the six-membered ring of CHA is performed and the potential energy landscape is given in Fig. (4.2).

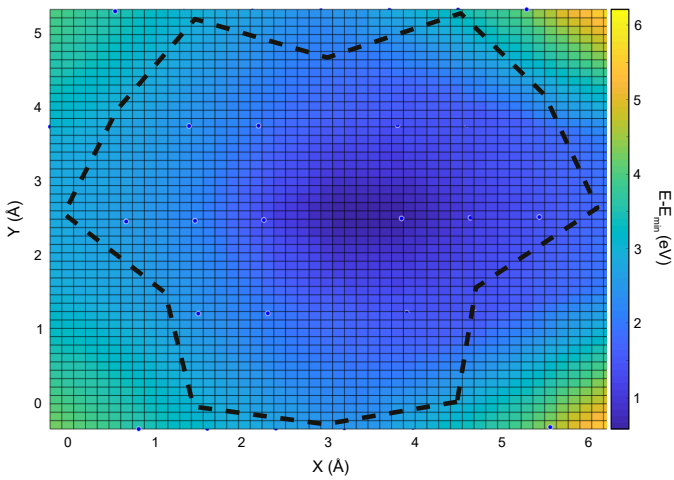

Figure 4.2: Potential energy landscape for Cu on the six-membered ring of CHA. The energies are given with respect to minima for Cu. The black dashed line represented the six-membered ring of CHA and the blue dots are the sampling points.

The comparison between the entropy of framework Cu from harmonic approximation and CPES method shows that the harmonic approximation results in an overestimation

of the entropy by 9.7 J/K in the investigated temperature range (200 - 900K). Thus, in the thesis we adopted the CPES results.

4.1.3 Entropy for mobile molecules in CHA

When molecules are present in the zeolites, they are restricted as compared to gas-phase molecules, although they still have a considerable degree of freedom. A common method to evaluate the entropy of the molecule in zeolite is treat them as adsorbates, where all degrees of freedom are treated as vibrations.[84] However, this method often underestimates the molecular entropy for species in zeolites as they are weakly bound and still maintain a part of translations and rotations.

By comparing with the CPES simulation mentioned in 4.1.2, it was found that for non-bound small molecules in zeolites, about 2/3 of their translational and rotational entropy in gas-phase should be retained.[34;84] Thus, the expression of entropy for the species in zeolite, S^{zeo}, is given by:

$$S^{\mathrm{zeo}} = S^{\mathrm{zeo}}_{\mathrm{vib}} + \gamma \left(S^{\mathrm{gas}}_{\mathrm{rot}} + S^{\mathrm{gas}}_{\mathrm{trans}}\right) \tag{4.14}$$

Where $S^{\mathrm{zeo}}_{\mathrm{vib}}$ is the vibrational entropy calculated in the zeolite. γ is the effective coefficient and it was set as 2/3 for non-bound small molecules in zeolites. However, for the bulky molecules, they are likely to be more significantly hindered by the zeolite structure, γ should be reduce.

4.2 NH_3-temperature programmed desorption simulations

One way to verify the entropy calculations is to compare with temperature programmed desorption (TPD) experiments. In this thesis, NH_3-TPD was used in this way. Experimentally, NH_3-TPD is a method to determine the bond strength of acid sites in zeolite. Following the method proposed in previous works,[85;86] we simulated NH_3-TPD profiles. In this section, the method of simulation and the way we determined the effective coefficient in eq. (4.14) will be presented.

4.2.1 Evaluation of NH_3-TPD

The simulation of NH_3-TPD is based on the equilibrium between the gas-phase NH_3 and the adsorbed NH_3:

$$\mathrm{NH_3^*} \underset{k_a}{\overset{k_d}{\rightleftharpoons}} \mathrm{NH_3(g)} + * \tag{4.15}$$

Where * is the adsorption site and NH_3(g) is the gas-phase ammonia. The adsorption and desorption rate constants are denoted by k_a and k_b, respectively. When taking the re-adsorption into account, the corresponding rate equation is:

$$\frac{d\theta}{dt} = k_a \frac{p_{\mathrm{g}}}{p^0}(1-\theta) - k_d\theta \tag{4.16}$$

Here θ is the NH_3 coverage, p_g is the pressure of NH_3, and p^0 is the standard atmospheric pressure. Combining the ideal gas law ($pV = k_BT$) with eq. (4.16), the concentration of NH_3 can be presented as:

$$C_g = \frac{\theta}{1-\theta}\frac{p^0}{k_BT}K \tag{4.17}$$

Where K is the equilibrium constant that can be evaluated by the enthalpy and entropy changes (ΔH and ΔS):

$$K = \frac{k_a}{k_d} = \exp\left(-\frac{\Delta H}{k_BT}\right)\exp\left(\frac{\Delta S}{k_BT}\right) \tag{4.18}$$

In this thesis, the ΔH is approximated as the differential desorption energy with zero point correction of NH_3 from the adsorption sites in Cu-CHA. The change in entropy (ΔS) is the difference in entropy before and after each desorption step.

In the TPD experiments, the amount of NH_3 that enter and exit from the catalyst can be measured and the mass balance is given by:

$$FC_g = -A_0W\frac{d\theta}{dt} \tag{4.19}$$

where F, A_0, and W are the flow rate of the carrier gas, the number of sites per weight catalyst and the weight of the catalyst, respectively. Owing to the linearly increase of temperature in the TPD, the relation between the change in time and temperature is $dT = \beta dt$. β is the heating rate. In this way, the expression of C_g can be written by:

$$C_g = -\frac{\beta A_0W}{F}\frac{d\theta}{dt} = \frac{\theta}{1-\theta}\frac{p^0}{k_BT}\exp\left(-\frac{\Delta H}{k_BT}\right)\exp\left(\frac{\Delta S}{k_BT}\right) \tag{4.20}$$

The concentration as a function of temperature is solved numerically by stepping the coverage:

$$\theta_{i+1} = \theta_i + \left(\frac{d\theta}{dT}_i\right)\Delta T \tag{4.21}$$

4.2.2 Determination of γ by fitting to experimental NH_3-TPD

In the NH_3-TPD simulation, the change in enthalpy of each desorption step is calculated through DFT including the zero-point correction. The entropy of each species is evaluated by the methods introduced in section 4.1.

The NH_3-TPD of Brønsted acid sites can be obtained by TPD measurements from H-CHA. As a weakly bound molecule, the evaluation of NH_4^+ entropy should follow eq. (4.14). In the first attempt, γ was set to 2/3 according to the previous studies,[34;84] and the comparison between experiment and simulation curves is shown in Fig. 4.3(a). It can be seen that there is a clear difference between the experimental and the simulation curve where the simulated desorption peak appear at higher temperatures. This results indicated that the entropy of NH_4^+ is overestimated within this approximation. By reducing the γ value, the desorption peak shifts to lower temperature and agree with the experimental desorption temperature when γ is set to 0.29 which in shown in Fig. 4.3(b and c).

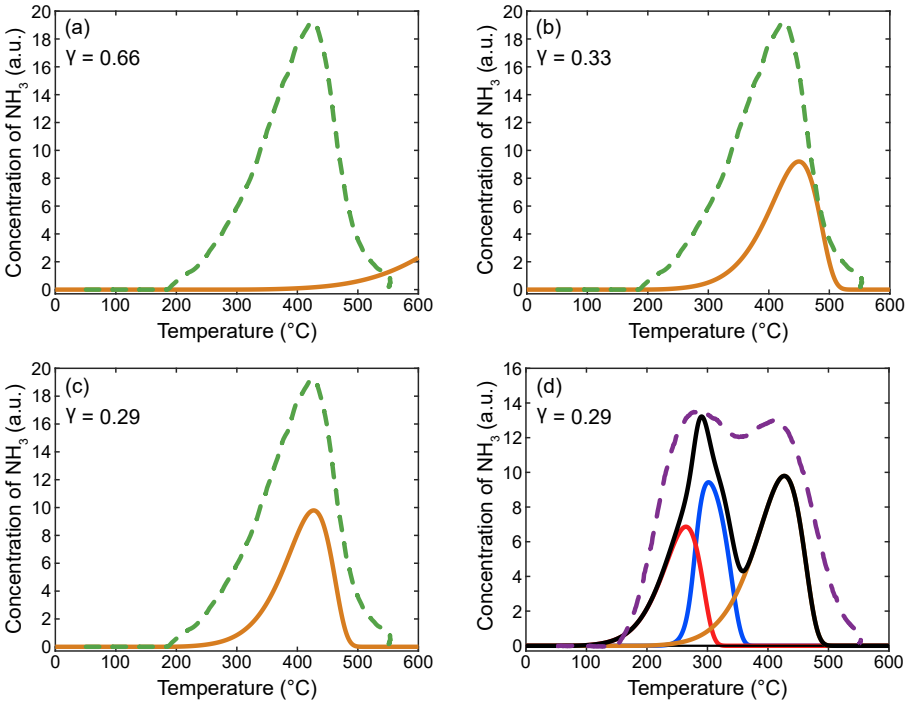

Figure 4.3: Simulated and experimental NH_3 desorption profiles in H-CHA(a, b and c) and Cu-CHA(d). The experimental profiles (green dashed line and purple dashed lines) is measured after NH_3 adsorption at 70 °C. The simulated profiles contains the NH_3 desorption from Brønsted acid site (orange lines), $[Cu(NH_3)]^+$ (blue line), $[Cu(NH_3)_2]^+$ (red line), and the sum of NH_3 desorption from each sites(black line). The experiment data is provided by Ton V.W. Janssens, Umicore.

Owing to the difference in the mobility between complexes, the simulation of the NH_3-TPD from the Cu site is more complicated. In the entropy evaluation part, the entropy of framework Cu is calculated by the CPES method. $[Cu(NH_3)]^+$ is evaluated by the harmonic approximation with 12 vibrational modes. The rest of the complexes are calculated following eq. (4.14). Similar fitting as for NH_3-TPD of Brønsted acid sites have been performed to get a reasonable γ value. It is interesting to note that $\gamma = 0.29$ also provides a good fit as it shown in Fig. 4.3(d).

4.2.3 Entropy change for O_2 absorption over Cu-CHA

Oxygen adsorption over a pair of $[Cu(NH_3)_2]^+$ complexes is a key step in NH_3-SCR.[87] Through the adsorption process, $[Cu_2(NH_3)_4O_2]^{2+}$ complex forms (shown in Fig. 4.4) and allows the $Cu^I \rightarrow Cu^{II}$ oxidation. It is worth noting that as the complexes before and after the adsorption are both relatively mobile, the entropy change during this process is

difficult to estimate by conventional methods. In this thesis, we used the γ value from 4.2.2 to evaluated the entropies of $[Cu(NH_3)_2]^+$ and $[Cu_2(NH_3)_4O_2]^{2+}$ complex. Furthermore, the entropy differences of O_2 adsorption in the forward (ΔS_f^{zeo}) and backward reaction (ΔS_b^{zeo}) were evaluated by:

$$\Delta S_f^{\text{zeo}} = S^{\text{zeo}}_{\text{TS},[Cu_2(NH_3)_4O_2]^{2+}} - (2\, S^{\text{zeo}}_{[Cu(NH_3)_2]^+} + S^{\text{gas}}_{O_2}) \tag{4.22}$$

$$\Delta S_b^{\text{zeo}} = S^{\text{zeo}}_{\text{TS},[Cu_2(NH_3)_4O_2]^{2+}} - S^{\text{zeo}}_{[Cu_2(NH_3)_4O_2]^{2+}} \tag{4.23}$$

$S^{\text{zeo}}_{\text{TS},[Cu_2(NH_3)_4O_2]^{2+}}$ and $S^{\text{zeo}}_{[Cu_2(NH_3)_4O_2]^{2+}}$ are the entropies of the transition and final state configurations of the adsorption, respectively. $S^{\text{zeo}}_{[Cu(NH_3)_2]^+}$ is the entropy of the $[Cu(NH_3)_2]^+$ complex in the zeolite.

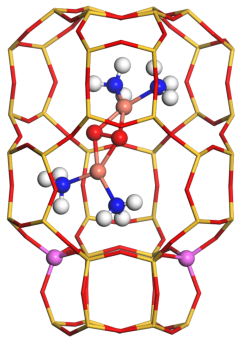

Figure 4.4: Side view of the chabazite cages showing the Al positions in the six-membered ring. The large cage includes the $[Cu_2(NH_3)_4(O_2)]^{2+}$ complex.

In the recent experimental work of the O_2 adsorption on a pair of $[Cu(NH_3)_2]^+$ complexes, the entropy loss was measured to be 142 J/mol $\cdot$ K.[88] With the method proposed above, our computational estimate is 152 J/mol $\cdot$ K, which shows a good agreement with the measured entropy change. The successful evaluation of entropy loss from first principles calculation further validates the obtained γ value obtained by fitting with experimental NH_3-TPD.

Chapter 5

Microkinetic modeling

First principles-based reaction kinetics makes it possible to establish connections between experiments and atomistic simulations. Moreover, this kind of simulations provides detailed insights that are difficult to obtain from experiments alone. This chapter describes the basic of mean-field kinetic models.

5.1 Microkinetic modeling

Mean-field microkinetic modeling is here used to simulate reaction kinetics. The basic mean-field approximations are that all adsorbates are distributed randomly over the surface and that the interactions between the adsorbates are small.[73 (p. 52)] However, repulsive interactions can be handled, and such dependence on pre-exponential factors and activation energy has been taken into account. The equilibrium reaction rate and coverages are in the mean-field approach achieved by the numerical solutions of a set of coupled ordinary differential equations. The differential equation that describe the time evolution if the adsorbate coverages of species i can be written as:

$$\frac{d\theta_i}{dt} = \sum_j r_j(\overrightarrow{\theta})c_{ij} \tag{5.1}$$

Here θ_i is the fractional coverage of species i and the rate of reaction j is represented by r_j. r_j depends on the fractional coverages ($\overrightarrow{\theta}$). c_{ij} is the number of i-molecules consumed in reaction j. I used the ode23s solver within MATLAB to integrate the system of differential equations numerically until steady-state is reached. According to eq. (3.5) and eq. (3.6), the rate constant of each elementary step can be calculated by their respective changes in energy and entropy. For each elementary step, the net rate can be written as:

$$r_j = k_j^+ \prod_f \theta_f - k_j^- \prod_b \theta_b \tag{5.2}$$

Here f is the reactant species that participate in forward reaction of elementary step j, while b represented the backward reaction.

It is worth noting that the model is not built in a one-step process. Fig. 5.1 illustrate the workflow of how we constructed the model. The reaction mechanism was established based on experiments and DFT calculations. With the elementary steps and inputs (ΔE, ΔS), rate constant and the other kinetic data was obtained. By comparing experimental and simulated kinetics, the validly of the kinetic model was confirmed. In situations of the model with poor agreement, improvements was made to the mechanism and input, and the next round of rate constant calculation and comparison with experiments was made until an agreement was obtained.

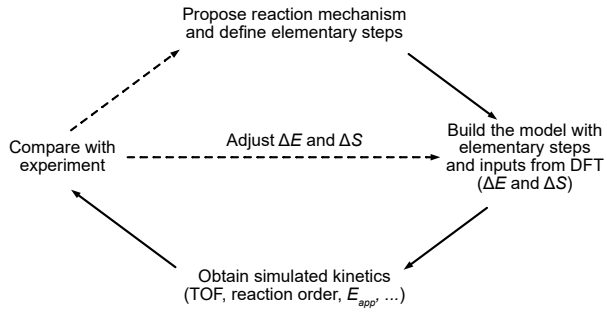

Figure 5.1: Illustration of the workflow for constructing a microkinetic model based on first principles calculations.

5.2 Analysis of reaction kinetics

One of the major roles of kinetic models is to provide kinetic data that can be compared with experimental measurements and in this way validate proposed reaction paths. This section will focus on the data that can be generated and the analysis that can be performed based on kinetic models.

5.2.1 Turnover frequency and coverage

The turnover frequency (TOF) is defined as the number of reactant molecules that are converted over one site per second.[73 (p.174)] As the net rate from the kinetics can also represent the reactant consumption and product formation, the TOF can be obtained by summing up the rate of elementary steps that generate the product molecule. Generally, there could be a large difference in numerical values between the experimental results and the simulated TOFs due to the approximations and uncertainties in the model. However, the trend of TOF affected by reaction conditions like temperature and reactant concentration should agree with experimental results for the model to be valid.

It is worth noting that TOF is not the only criterion to judge catalyst efficiency. The selectivity is also of great importance. In the kinetic model, the selectivity of the target product is the ratio of product yield to the TOF of the reactant.

The coverage of each potential species could be obtained directly by solving eq. (5.1) and the coverage should sum up to the saturating coverage. The comparison between the simulated most abundant species and experimental spectroscopy measurement is helpful to determine the validity of the model and can be used for the adjustment of the parameters in the model.

5.2.2 Reaction order and apparent activation energy

The reaction orders and apparent activation energies are commonly used to characterize catalytic reactions experimentally and computationally. Based on the rate equation,[73 (p.38-41)] the relationship between rate r, rate constant k, and the concentration of the reactants

can be expressed as:

$$r = k \prod_i p_i^{n_i} \tag{5.3}$$

where p_i is the partial pressure of species i and n_i is the reaction order of i. In both experiments and simulations, the reaction order of reactant i can be evaluated by studying the variation of reaction rate (or TOF) at a certain pressure gradient of i when the pressure of the other reactants are kept fixed.

By combining the Arrhenius equation shown in eq. (3.4) and eq. (5.3), the following equation is obtained:

$$r = A \exp\left(-\frac{E_{app}}{k_B T}\right) \prod_i p_i^{n_i} \tag{5.4}$$

here E_{app} is the apparent activation energy. In experiments, the natural logarithm is generally taken for both side of the reaction to plot a figure of $\ln r$ vs $1/T$ as shown in Fig. 5.2, which provides apparent activation energy.

Within a narrow temperature range, the plot of $\ln r$ vs $1/T$ will be presented as a straight line and the slope is equal to $-E_{app}/k_B$.

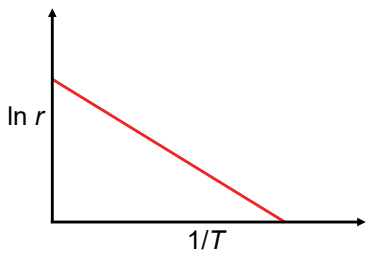

Figure 5.2: Schematic of an Arrhenius plot, yielding the apparent activation energy as the slope.

5.2.3 Degree of rate control

The success of a kinetic model can be determined by comparison of the simulated TOF and reaction order with experimental results. With a successful model, it is desirable to further analyze the effect of each elementary steps on the overall reaction. To achieve this, the degree of rate control (χ_i) analysis that can be used to understand the extent to which a particular elementary step determines the simulated catalytic rate.[89;90] The calculation of χ_i is performed as:

$$\chi_i = \frac{k_i}{r} \left(\frac{\partial TOF}{\partial k_i}\right)_{K_i} \tag{5.5}$$

Here k_i is the rate constant of step i and K_i is the equilibrium constant. The analysis is carried out by changing the value of rate constants for the forward and backward reaction

for each elementary step a small amount (1% in this thesis) while keeping the equilibrium constant and the rate constants of all the other steps constant. The value of χ shows the relative importance of each elementary reaction and the step that have largest χ can be considered as the rate determining step at that particular reaction condition. The sum of χ_i for a single branch reaction should be one.

Chapter 6

Microkinetic model for NH_3-SCR over Cu-CHA

In Chapter 1, we stressed the importance to reduce N_2O emissions during the NH_3-SCR. However, the research on the reaction mechanism of N_2O formation over Cu-CHA is still limited. This chapter will first discuss the results from a N_2O formation mechanism study (**Paper I**) in which we proposed a low barrier N_2O formation path over Cu-site, which is in line with experimental observations. To investigate the kinetic of NH_3-SCR over Cu-CHA and explore ways to promote the activity as well as selectivity to N_2, a first principles microkinetic model including N_2O formation was developed (**Paper II**). The results and analysis from the microkinetic model will also be discussed in this chapter.

6.1 N_2O formation during NH_3-SCR over Cu-CHA

According to the proposed reaction cycles (see Ref. 34 and Fig. 6.2), the NH_3-SCR reaction starts with O_2 adsorption over the $[Cu(NH_3)_2]^+$ pairs forming Cu-peroxo, $[Cu_2(NH_3)_4O_2]^{2+}$. Following that, NH_3 and NO react over the Cu-peroxo yielding H_2NNO and $[Cu_2(NH_3)_4OOH]^{2+}$ complex. The H_2NNO intermediate diffuses to Brønsted acid site and decomposes into N_2 and H_2O with the assistance of ammonium (NH_4^+). Based on the similar onset temperature of N_2 and N_2O formation in NH_3-SCR observed experimentally, it is reasonable to suppose a N_2O formation path that occur over the same active site as N_2 formation and has a similar reaction barrier.

In **Paper I**, the decomposition of the H_2NNO intermediate over $[Cu_2(NH_3)_4OOH]^{2+}$ was investigated. It was found that the protons on H_2NNO easily can transfer to the -OOH group of $[Cu_2(NH_3)_4OOH]^{2+}$. This reaction path involves spin-flip processes due to the changes of oxidation state over the Cu cations. When the spin state of Cu is allowed to change along the reaction, this path is barrierless as shown in Fig. 6.1(b). To confirm the reaction barrier, a spin constrained simulation was performed giving an activation barrier of 0.24 eV. N_2O and H_2O are generated after the sequential proton transfers and the Cu active goes to $[Cu_2(NH_3)_4OH]^{2+}$, which is also a state within the reaction cycles.[34] Therefore, this N_2O formation path can be coupled to the original reaction cycle as a side reaction, and provide a possibility for calculating selectivity of N_2O from the kinetic model.

6.2 Establishment of the microkinetic model

Based on the proposed reaction cycle (marked by black arrows in Fig. 6.2 and the N_2O formation path (marked by red dashed arrow in Fig. 6.2), a microkinetic model was

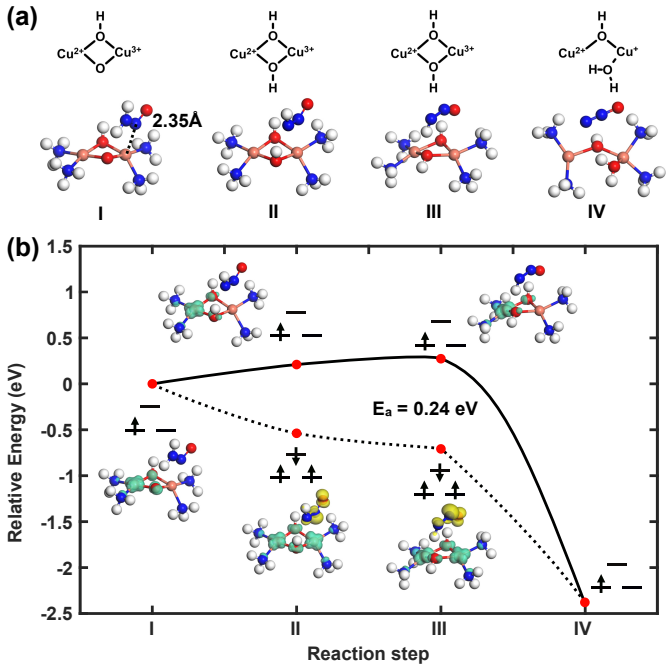

Figure 6.1: (a) Structures of key configurations in the N_2O formation over a $[Cu(NH_3)_2\text{-}OOH\text{-}(CuNH_3)_2]^{2+}$ complex and (b) the corresponding reaction landscape. The spin configurations are schematically shown by arrows in (b). The two lower states refer to the two Cu atoms, whereas the single upper state refers to the electronic state of the adsorbate (H_2NNO, HNNO, or N_2O). The formal charges on the Cu-ions following the least stable potential energy curve (solid line) are show in (a). The molecular structures in (b) show the spin density at an iso-surface of 0.09 e/Å^3. Atomic color codes: H (white), N (blue), O (red), and Cu (bronze).

developed and an analysis of the reaction kinetics was performed to allow for comparisons with experiments. Generally, the coverage, θ_i, is defined as the ratio of species i to the number of sites. However, in the kinetic model in this thesis, the fractional coverages is understood as the fraction of Cu-site being in a certain state of the reaction cycle.

In the initial attempt, the adopted ΔE and ΔS are all from DFT calculations. However, these values results in an extremely low fractional coverage of Cu-peroxo and a low TOF. While in the experiment,[87] it shows that with a sufficient amount of $[Cu(NH_3)_2]^+$, the adsorption of O_2 should be possible. To improve the model and achieve a better agreement with the experiments, some corrections and additions of the model were made.

6.2.1 Correction of the underestimated O_2 adsorption energy

The low fractional coverage of Cu-peroxo originates from the underestimated adsorption energy of O_2 (0.2 eV) in the DFT calculations. To improve the kinetic model, the recent

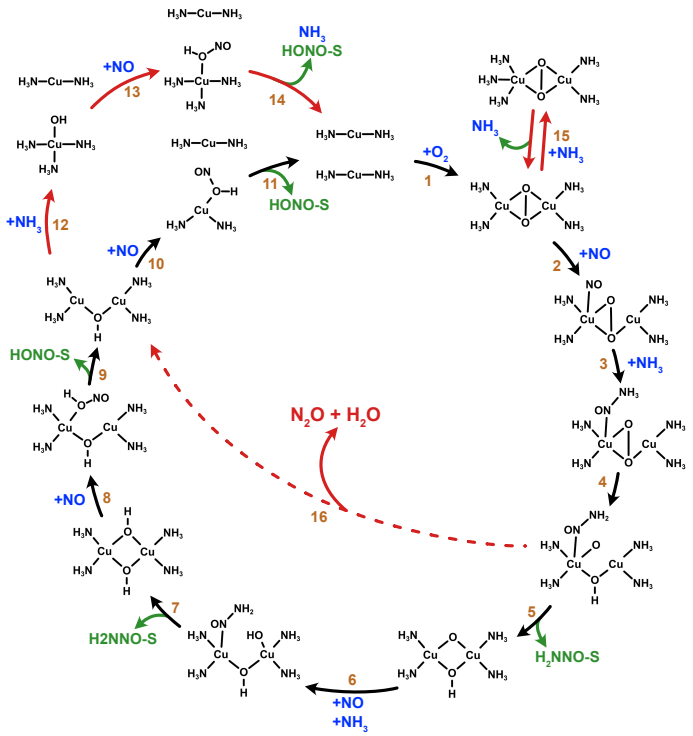

Figure 6.2: Proposed reaction cycle for low-temperature NH_3-SCR over Cu-CHA.

reported experimental value of 0.82 eV in Ref. 88 was adopted as a correction. The different of O_2 adsorption energy between calculated and experimental can be attributed to the difficulty describing properly O_2 in the gas phase with the exchange-correlation that applied in this work and the arbitrariness of initial state for the $[Cu(NH_3)_2]^+$ pairs. By adopting experimental value for O_2 adsorption, this elementary step can be conducted at a plausible forward reaction rate and the subsequent steps in the second version of the model were able to proceed. However this model did not agree with experimental light-off measurements and reaction orders.

6.2.2 Inclusion of the NH_3 blocking step

In experiments,[15;91] that have an NH_3/NO ratio close to 1, the reaction order with respect to NH_3 is zero or slightly negative and the apparent activation energy for NH_3-SCR has been reported to be about 0.4 to 0.8 eV. However, this model gives a positive reaction order (0.05) for NH_3 and a relatively low apparent activation barrier of 0.31 eV. These results indicate that NH_3 should have a hindering effect on the reaction in the experiment with the second version of the model did not reproduce.

Recent experimental work over the Cu-peroxo observed that excess NH_3 can adsorb

on the Cu-peroxo leading to a partial reduction of Cu.[92] Related DFT calculations were performed in this thesis and it was shown that the extra NH_3 on the Cu site of Cu-peroxo (shown in Fig. 6.3) have an adsorption energy of 0.98 eV, which is higher than NO ($E_{ads-NO} = 0.70$ eV). More importantly, NO is not be able to react over this $[Cu_2(NH_3)_5(O_2)]^+$ complex, which indicated that the adsorption of the extra NH_3 will hinder the NH_3-SCR reaction. Thus, the NH_3 adsorption step is added into the reaction cycle (r15) as a competitive step for NO adsorption in the third version of the model. With the hindering effect of NH_3, the reaction order with respect to NH_3 reduces to -0.22 and gives an apparent activation energy of 0.75 eV, which are in good agreement with experiments.

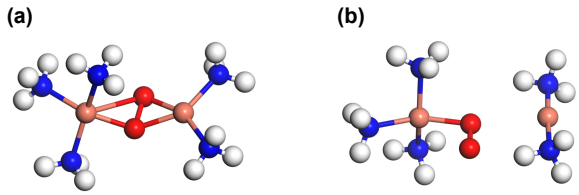

Figure 6.3: Two structures of $[Cu_2(NH_3)_5(O_2)]^{2+}$. Atom color codes: Cu (bronze), Si (yellow), Al (pink), O (red), N (blue) and H (white).

The analysis of fractional coverage and degrees of rate control indicated that the rate of NH_3-SCR is mainly determined by NO adsorption, which is hinder by the inhibiting-NH_3. Given that the potential energy surface of the proposed reaction mechanism is flat, it is the adsorption of inhibiting-NH_3 that actually determines the reaction rate and mainly contributes to the apparent activation energy.

6.2.3 Consideration of the probability for Cu pairing

With the correction of O_2 adsorption energy and the inclusion of NH_3 blocking step, the microkinetic model was consistent with experimental kinetic data. However, the absolute value of the calculated TOF, although following the experimental trend, was significantly overestimated. To close the gap between simulation and experiment, the probability of having Cu pair in the same cage was also taken into account. The third kinetic model (6.2.2) was based on having a pair of $[Cu(NH_3)_2]^+$ in the same cage and once O_2 has been adsorbed, the sequential elementary steps start. However, as reported in previous work,[87] a certain energy difference exists to have two complexes in the same cage rather than in different cages. In this thesis the barrier was estimated to be 0.3 eV,[87] which corresponds to a probability of 6×10^{-4} having two complexes in the same cage.

After taking the probability of having two Cu-complexes in the same CHA cage into consideration, simulated TOFs that comparable with experimental values were obtained. The experimental fits over the reaction order measurements for 1.6 wt% Cu-CHA sample and the TOFs evaluated from the first principles microkinetc model was shown in Fig. 6.4. The TOFs from the model is simulated with the similar reaction conditions as the experiments for reaction order measurements.

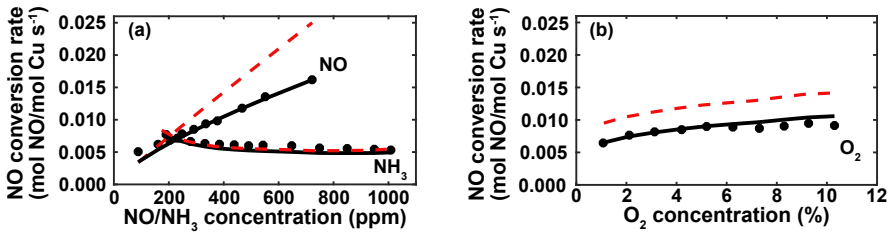

Figure 6.4: Experimental reaction rate (black dots) over the 1.6 wt% Cu-CHA sample and simulated TOFs (red dashed line) versus the concentration of (a)NO, NH_3, and (b) O_2 at 200 °C. The experiment data is provided by Xueting Wang from the Competence Centre for Catalysis at Chalmers and the experiment details are given in **Paper II**.

The comparisons show a very good agreement on both the reaction orders and reaction rates. For NH_3, the experimental and simulated curves basically overlap. For oxygen, the trend is consistent although the rates are slightly overestimated in the simulations. For the simulated TOF of NO, it fits at low NO concentrations but starts to divide with increasing concentrations. We attribute this overestimation to the lack of possible side reactions in the model that consumes NO without producing any N_2. Nevertheless, the experimental and computational TOFs are within a factor of 2, which confirms the validity of the model.

6.2.4 The effect of Cu/Al ratio and O_2 pressure

The successful establishment of the microkinetic model provides the possible to predict experimental phenomena through the model. One of the issues that has received widespread attention is the effect of Cu/Al ratio. In the proposed reaction cycle, the selectivity of N_2O is based on the probability of the reaction following r5 or r16 (Fig. 6.2). Moreover, as the NH_3-SCR reaction requires both the Cu sites and Brønsted acid sites, while N_2O formation only needs the Cu sites, the selectivity of N_2O should be affected by the Cu/Al ratio.

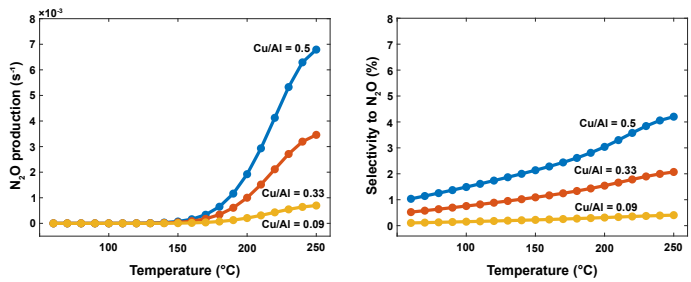

Figure 6.5: Simulated N_2O production (top) and selectivity (bottom) over Cu-CHA with different Cu/Al ratios.

In our model, the Cu/Al ratio was set to 0.5 which gives an N_2O selectivity of 4 % at 250 °C. We further modeled the formation of N_2O with different Cu/Al ratio (shown in Fig. 6.5). When the Cu/Al ratio decreases, selectivity also shows a decreasing trend which is matches the experimental observation.

On the other hand, the reaction order with respect to O_2 has been measured to be reduced with increasing O_2 pressure.[93] A series of simulations with Cu/Al ratio of 0.23 which is the same as in the experiment were conducted and shown in Fig. 6.6. The results show that our kinetic model closely follows the experimental results while the simulated rate at low pressures increases steeper than the experiment. This phenomenon could be attributed to the overestimation of the formation of the peroxo species at low temperatures as well as that all Cu-sites may not be used experimentally.

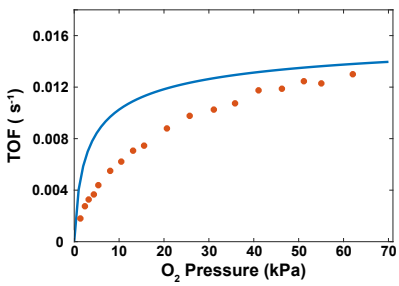

Figure 6.6: Turnover frequency of NO consumption over Cu-CHA with a Cu/Al ratio of 0.23 using the cycle in Fig. 6.2 (solid line). The experiments (dots) are taken from Ref. 93. The simulations and experiments are performed at a temperature of 473 K with partial pressures of NO and NH_3 being both 0.03 kPa.

Chapter 7

Conclusions and outlook

The main aim of this thesis is to investigate the reaction kinetics of low-temperature NH_3-SCR over Cu-CHA by establishing a first principles microkinetic model. To achieve this aim, different attempts have been made to refine the a previously proposed reaction mechanism and evaluate the entropy. After several iterations, the model achieved good agreement with the experiment and provided new insights for further understanding of NH_3-SCR over Cu-CHA.

To start with, a N_2O formation path that can be coupled in the multisite mechanism was proposed. The low reaction barrier and critical role of Cu-site for the proposed path provided an explanation for the nearly simultaneous emission peaks of N_2 and N_2O that observed in experiments.

Following that, a first principles microkinetic model was developed. To obtain rate constants that can reflect the actual situation of the elementary steps, delicate estimations of the entropy were performed. The simulation of NH_3-TPD was introduced to assist in determining the accuracy of evaluated entropies. By fitting to experimental NH_3-SCR, the validity of the methods used to estimate entropy was confirmed. Similar method was used to evaluate the entropy loss of O_2 adsorption over $Cu(NH_3)_2$ pairs, which showed a good agreement with experimental measurement. Through comparisons with experiments, our model was revised by adopting the experimental adsorption energy of O_2, adding the NH_3 inhibition effect, and the considering the possibility of having a pair of $Cu(NH_3)_2$ complexes in the same cage. The final version of the model reached a good agreement with the experimental kinetics.

By comparing the models with the presence and absence of inhibiting-NH_3, the significant impact of NH_3 on the NH_3-SCR was revealed. The analysis of coverage and the degree of rate control further uncovered how the inhibiting-NH_3 determine the onset temperature of NH_3-SCR. With the model, it can be concluded that the reaction cycles contain four types of NH_3, with different roles in the low-temperature NH_3-SCR reaction:

1. Ligand-NH_3: NH_3 that adsorbs on the Cu-cations, forming mobile $[Cu(NH_3)_2]^+$ complexes, which enable facile formation of pairs for O_2 adsorption. The ligand-NH_3 does not participate in the low-temperature SCR reaction provided that NH_3 is in excess.

2. Inhibiting-NH_3: NH_3 that adsorbs strongly on the $[Cu_2(NH_3)_4O_2]^{2+}$ species, and thereby blocks the adsorption of NO, which is required for NH_3 SCR reaction.

3. Reactant-NH_3: NH_3 that takes part in the reaction by reacting with NO.

4. NH_4^+: NH_3 that is adsorbed at the Brønsted acid sites forming NH_4^+.

In low-temperature NH_3-SCR, NH_3 acts simultaneously as reactant, spectator and inhibitor. It is close to impossible to obtain such information by experiment alone, which shows the significance and necessity of developing microkinetic models.

7.1 Outlook

By introducing a factor that reflects the probability of having a pair of $Cu(NH_3)_2$ complexes in the same cage, the kinetic model provided a reaction rate that is close to the experimental value. However, the dependence of this factor on Cu/Al ratios, and Al distribution is still not accounted for. As a next step, we would like to explore these effects.

Although the model can reproduce experimental data fairly well, it is only valid for low temperature NH_3-SCR. As the temperature increases, the NH_3 ligands on the Cu-complexes desorb and Cu will gradually exist in the form of framework bound Cu. The mechanism of NH_3-SCR and N_2O formation over framework bound Cu is still unclear and is not included in our model. Therefore, work is needed to explore the reaction mechanisms and develop a microkinetic model for high-temperature NH_3-SCR. In addition, there are experiments showing that water has an effect on the activity and the selectivity of the NH_3-SCR, which is not considered in our model but could be a topic for future studies.

Acknowledgments

The research was carried out at the Division of Chemical Physics and Competence Centre for Catalysis at Chalmers University of Technology, Göteborg, Sweden in the period August 2019 to October 2021.

The research is funded by the Swedish Energy Agency through an FFI-project (47110-1).

The Competence Centre for Catalysis is hosted by Chalmers University of Technology, and financially supported by the Swedish Energy Agency, and the member companies: AB Volvo, ECAPS AB, Johnson Matthey AB, Preem AB, Scania CV AB, and Umicore Denmark Aps.

Computational time was granted by SNIC at C3SE (Göteborg) and PDC (Stockholm).

In addition, I would like to thank:

My main supervisor, Henrik Grönbeck. Thank you for always answering my questions patiently and giving me advice to find my way and get back on track. I appreciate that you always listen to and encourage me!

My co-supervisor, Magnus Skoglundh, and Anders Hellman for the discussions and encouragement at all the presentations.

All my colleagues at Chemical Physics and KCK are gratefully acknowledged. Thank you for creating a warm and nice working environment (and the best fika). I am happy to meet all of you in the corridor or through the window of my office because your smiles always brighten up my day.

I would also like to especially thank Lin, you are a wonderful officemate and have given me lots of help. Looking forward to see you again at Chalmers.

All my Chinese friends at Chalmers, especially Jojo and Ze, for all the care, great moments, and interesting discussions.

Mei, for being my biggest fan and trying to cheer me up at all the tough moments. And of course my mum and dad, it would be impossible for me to go this far without your support, and thank you so much for loving me enough to set me free.

Yingxin Feng, Göteborg, November 2021

Bibliography

[1] Twigg, M. V. Progress and Future challenges in Controlling Automotive Exhaust Gas Emissions. *Appl. Catal. B Environ.*, *70* (2007), 2–15. ISSN 09263373. doi: 10.1016/j.apcatb.2006.02.029.

[2] Sourses of Air Polution in Europe. [EB/OL]. `https://www.eea.europa.eu/themes/air/air-pollution-sources-1`.

[3] Lashof, D. A. and Ahuja, D. R. Relative Global Warming Potentials of Greenhouse Gas Emissions. *Nature*, *344* (1990), 529–531.

[4] [EB/OL]. `https://www.dieselforum.org/about-clean-diesel/what-is-scr/`.

[5] Emissions of Air Pollutants from Transport. [EB/OL]. `https://www.eea.europa.eu/data-and-maps/indicators/transport-emissions-of-air-pollutants-8/transport-emissions-of-air-pollutants-8`.

[6] Johnson, T. V. Diesel Emission Control in Review. *SAE Tech. Pap.*, *1* (2001), 68–81. ISSN 26883627. doi: 10.4271/2001-01-0184.

[7] Seinfeld, J. H. Air Pollution: A Half Century of Progress. *AIChE J.*, *50* (2004), 1096–1108. ISSN 00011541. doi: 10.1002/aic.10102.

[8] European Emission Standards. [EB/OL]. `https://eur-lex.europa.eu/legal-content/EN/TXT/?uri=CELEX:02011R0582-20191215#E0017`.

[9] Belton, D. N. and Taylor, K. C. Automobile Exhaust Emission Control by Catalysts. *Curr. Opin. Solid State Mater. Sci.*, *4* (1999), 97–102. ISSN 13590286. doi: 10.1016/S1359-0286(99)80017-5.

[10] Bosteels, D. and Searles, R. A. Exhaust Emission Catalyst Technology. *Platin. Met. Rev.*, *46* (2002), 27–36. ISSN 00321400.

[11] Kašpar, J.; Fornasiero, P.; and Hickey, N. Automotive: Catalytic Converters Current Status and Some Perspectives. *Catal. Today*, *77* (2003), 419–449.

[12] Nova, I. and Tronconi, E. *Urea-SCR Technology for DeNO$_x$ After Treatment of Diesel Exhausts*. Springer Science+Business Media New York, 2014.

[13] Chorkendorff, I. and Niemantsverdriet, J. W. *Concepts of Modern Catalysis and Kinetics*. John Wiley & Sons, 2017.

[14] Dumesic, J. A.; Huber, G. W.; and Boudart, M. Principles of Heterogeneous Catalysis. In Handbook of Heterogeneous Catalysis. (2008), 1–26. doi: 10.1002/9783527610044.hetcat0001. URL `https://doi.org/10.1002/9783527610044.hetcat0001`.

[15] Gao, F.; Mei, D.; Wang, Y.; Szanyi, J.; and Peden, C. H. Selective Catalytic Reduction over Cu/SSZ-13: Linking Homo- and Heterogeneous Catalysis. *J. Am. Chem. Soc.*, *139* (2017), 4935–4942. ISSN 15205126. doi: 10.1021/jacs.7b01128.

[16] Chen, F.; Jiang, X.; Zhang, L.; Lang, R.; and Qiao, B. Single-Atom Catalysis: Bridging the Homo- and Heterogeneous Catalysis. *Chinese J. Catal.*, *39* (2018), 893–898. ISSN 02539837. doi: 10.1016/S1872-2067(18)63047-5. URL `http://dx.doi.org/10.1016/S1872-2067(18)63047-5`.

[17] Forzatti, P. Present Status and Perspectives in De-NO_x SCR Catalysis. *Appl. Catal. A Gen.*, *222* (2001), 221–236. ISSN 0926860X. doi: 10.1016/S0926-860X(01)00832-8.

[18] Chen, B. and Kan, H. Air Pollution and Population Health: A Global Challenge. *Environ. Health Prev. Med.*, *13* (2008), 94–101. ISSN 1342078X. doi: 10.1007/s12199-007-0018-5.

[19] Grossale, A.; Nova, I.; Tronconi, E.; Chatterjee, D.; and Weibel, M. NH_3-NO/NO_2 SCR for Diesel Exhausts Aftertreatment: Reactivity, Mechanism and Kinetic Modelling of Commercial Fe- and Cu-Promoted Zeolite Catalysts. *Top. Catal.*, *52* (2009), 1837–1841. ISSN 10225528. doi: 10.1007/s11244-009-9354-6.

[20] Xin, Y.; Li, Q.; and Zhang, Z. Zeolitic Materials for DeNO_x Selective Catalytic Reduction. *ChemCatChem*, *10* (2018), 29–41. doi: 10.1002/cctc.201700854.

[21] Jeon, J.; Lee, J. T.; and Park, S. Nitrogen Compounds (NO, NO_2, N_2O, and NH_3) in NO_x Emissions from Commercial EURO VI Type Heavy-Duty Diesel Engines with a Urea-Selective Catalytic Reduction System. *Energy and Fuels*, *30* (2016), 6828–6834. ISSN 15205029. doi: 10.1021/acs.energyfuels.6b01331.

[22] Kröcher, O. and Elsener, M. Chemical Deactivation of V_2O_5/WO_3-TiO_2 SCR Catalysts by Additives and Impurities from Fuels, Lubrication Oils, and Urea Solution. I. Catalytic Studies. *Appl. Catal. B Environ.*, *77* (2008), 215–227. ISSN 09263373. doi: 10.1016/j.apcatb.2007.04.021.

[23] Englund, J.; Dahlin, S.; Schaefer, A.; Xie, K.; Andersson, L.; Shwan, S.; Carlsson, P. A.; Pettersson, L. J.; and Skoglundh, M. Deactivation of a Vanadium-Based SCR Catalyst Used in a Biogas-Powered Euro VI Heavy-Duty Engine Installation. *Catalysts*, *10* (2020). ISSN 20734344. doi: 10.3390/catal10050552.

[24] Schildhauer, T. J.; Elsener, M.; Moser, J.; Begsteiger, I.; Chatterjee, D.; Rusch, K.; and Kröcher, O. Measurement of Vanadium Emissions from SCR Catalysts by ICP-OES: Method Development and First Results. *Emiss. Control Sci. Technol.*, *1* (2015), 292–297. ISSN 21993637. doi: 10.1007/s40825-015-0023-x.

[25] Schmieg, S. J.; Oh, S. H.; Kim, C. H.; Brown, D. B.; Lee, J. H.; Peden, C. H.; and Kim, D. H. Thermal Durability of Cu-CHA NH_3-SCR Catalysts for Diesel NO_x Reduction. *Catal. Today*, *184* (2012), 252–261. ISSN 09205861. doi: 10.1016/j.cattod.2011.10.034.

[26] Davis, M. E. and Lobo, R. F. Zeolite and Molecular Sieve Synthesis. *Chem. Mater.*, *4* (1992), 756–768. ISSN 15205002. doi: 10.1021/cm00022a005.

[27] Armor, J. N. Metal-Exchanged Zeolites as Catalysts. *Microporous Mesoporous Mater.*, *22* (1998), 451–456. ISSN 13871811. doi: 10.1016/S1387-1811(98)00098-5.

[28] Brandenberger, S.; Kröcher, O.; Tissler, A.; and Althoff, R. *The State of the Art in Selective Catalytic Reduction of NO_x by Ammonia Using Metal-Exchanged Zeolite Catalysts*, volume 50. 2008. ISBN 0161494080. doi: 10.1080/01614940802480122.

[29] Kwak, J. H.; Tonkyn, R. G.; Kim, D. H.; Szanyi, J.; and Peden, C. H. Excellent Activity and Selectivity of Cu-SSZ-13 in the Selective Catalytic Reduction of NO_x with NH_3. *J. Catal.*, *275* (2010), 187–190. ISSN 00219517. doi: 10.1016/j.jcat.2010.07.031. URL `http://dx.doi.org/10.1016/j.jcat.2010.07.031`.

[30] Blakeman, P. G.; Burkholder, E. M.; Chen, H. Y.; Collier, J. E.; Fedeyko, J. M.; Jobson, H.; and Rajaram, R. R. The Role of Pore Size on the Thermal Stability of Zeolite Supported Cu SCR Catalysts. *Catal. Today*, *231* (2014), 56–63. ISSN 09205861. doi: 10.1016/j.cattod.2013.10.047. URL `http://dx.doi.org/10.1016/j.cattod.2013.10.047`.

[31] Beale, A. M.; Gao, F.; Lezcano-Gonzalez, I.; Peden, C. H.; and Szanyi, J. Recent Advances in Automotive Catalysis for NO_x Emission Control by Small-Pore Microporous Materials. *Chem. Soc. Rev.*, *44* (2015), 7371–7405. ISSN 14604744. doi: 10.1039/c5cs00108k.

[32] Fickel, D. W.; D'Addio, E.; Lauterbach, J. A.; and Lobo, R. F. The Ammonia Selective Catalytic Reduction Activity of Copper-Exchanged Small-Pore Zeolites. *Appl. Catal. B Environ.*, *102* (2011), 441–448. ISSN 09263373. doi: 10.1016/j.apcatb.2010.12.022. URL `http://dx.doi.org/10.1016/j.apcatb.2010.12.022`.

[33] Gao, F.; Kwak, J. H.; Szanyi, J.; and Peden, C. H. Current Understanding of Cu-exchanged Chabazite Molecular Sieves for Use as Commercial Diesel Engine $DeNO_x$ Catalysts. *Top. Catal.*, *56* (2013), 1441–1459. ISSN 10225528. doi: 10.1007/s11244-013-0145-8.

[34] Chen, L.; Janssens, T. V.; Vennestrøm, P. N.; Jansson, J.; Skoglundh, M.; and Grönbeck, H. A Complete Multisite Reaction Mechanism for Low-Temperature NH_3-SCR over Cu-CHA. *ACS Catal.*, *10* (2020), 5646–5656. ISSN 21555435. doi: 10.1021/acscatal.0c00440.

[35] Kubota, H.; Toyao, T.; Maeno, Z.; Inomata, Y.; Murayama, T.; Nakazawa, N.; Inagaki, S.; Kubota, Y.; and Shimizu, K. Analogous Mechanistic Features of NH_3-SCR over Vanadium Oxide and Copper Zeolite Catalysts. *ACS Catal.*, (2021), 11180–11192. ISSN 2155-5435. doi: 10.1021/acscatal.1c02860.

[36] Pérez-Ramírez, J.; Kapteijn, F.; Schöffel, K.; and Moulijn, J. A. Formation and Control of N_2O in Nitric Acid Production: Where Do We Stand Today? *Appl. Catal. B Environ.*, *44* (2003), 117–151. ISSN 09263373. doi: 10.1016/S0926-3373(03)00026-2.

[37] Zhang, D. and Yang, R. T. N_2O Formation Pathways over Zeolite-Supported Cu and Fe Catalysts in NH_3-SCR. *Energy Fuels*, *32* (2018), 2170–2182. ISSN 15205029. doi: 10.1021/acs.energyfuels.7b03405.

[38] Liu, B.; Yao, D.; Wu, F.; Wei, L.; Li, X.; and Wang, X. Experimental Investigation on N_2O Formation during the Selective Catalytic Reduction of NO_x with NH_3 over Cu-SSZ-13. *Ind. Eng. Chem. Res.*, *58* (2019), 20516–20527. ISSN 15205045. doi: 10.1021/acs.iecr.9b03294.

[39] Colombo, M.; Nova, I.; and Tronconi, E. Detailed Kinetic Modeling of the NH_3-NO/NO_2 SCR Reactions over a Commercial Cu-zeolite Catalyst for Diesel Exhausts After Treatment. *Catal. Today*, *197* (2012), 243–255. ISSN 09205861. doi: 10.1016/j.cattod.2012.09.002. URL `http://dx.doi.org/10.1016/j.cattod.2012.09.002`.

[40] Ciardelli, C.; Nova, I.; Tronconi, E.; Chatterjee, D.; Bandl-Konrad, B.; Weibel, M.; and Krutzsch, B. Reactivity of NO/NO_2-NH_3 SCR System for Diesel Exhaust Aftertreatment: Identification of the Reaction Network as a Function of Temperature and NO_2 feed content. *Appl. Catal. B Environ.*, *70* (2007), 80–90. ISSN 09263373. doi: 10.1016/j.apcatb.2005.10.041.

[41] Chaturvedi, S. and Dave, P. N. Review on Thermal Decomposition of Ammonium Nitrate. *J. Energ. Mater.*, *31* (2013), 1–26. ISSN 07370652. doi: 10.1080/07370652.2011.573523.

[42] Babrauskas, V. and Leggett, D. Thermal Decomposition of Ammonium Nitrate. *Fire Mater.*, *44* (2020), 250–268. ISSN 10991018. doi: 10.1002/fam.2797.

[43] Mihai, O.; Widyastuti, C. R.; Kumar, A.; Li, J.; Joshi, S. Y.; Kamasamudram, K.; Currier, N. W.; Yezerets, A.; and Olsson, L. The Effect of NO_2/NO_x Feed Ratio on the NH_3-SCR System over Cu-zeolites with Varying Copper Loading. *Catal. Letters*, *144* (2014), 70–80. ISSN 1011372X. doi: 10.1007/s10562-013-1133-0.

[44] Dirac, P. A. M. Quantum Mechanics of Many-electron Systems. *Proceedings of the Royal Society of London. Series A, Containing Papers of a Mathematical and Physical Character*, *123* (1929), 714–733.

[45] Born, M. and Oppenheimer, R. J. On the Quantum Theory of Molecules (English translation). *Ann. Phys.*, *457* (1927), 1–32. URL `http://www.ulb.ac.be/cpm/people/scientists/bsutclif/bornop.pdf`.

[46] Hohenberg, P. and Kohn, W. Inhomogeneous Electron Gas. *Phys. Rev.*, *136* (1964), B864–B871. doi: 10.1103/PhysRev.136.B864. URL `https://link.aps.org/doi/10.1103/PhysRev.136.B864`.

[47] Cohen, A. J.; Mori-Sánchez, P.; and Yang, W. Challenges for Density Functional Theory. *Chem. Rev.*, *112* (2012), 289–320. ISSN 00092665. doi: 10.1021/cr200107z.

[48] Kohn, W. and Sham, L. J. Self-Consistent Equations Including Exchange and Correlation Effects. *Phys. Rev.*, *140* (1965), A1133–A1138. doi: 10.1103/PhysRev.140.A1133. URL https://link.aps.org/doi/10.1103/PhysRev.140.A1133.

[49] Sousa, S. F.; Fernandes, P. A.; and Ramos, M. J. General Performance of Density Functionals. *J. Phys. Chem. A*, *111* (2007), 10439–10452. ISSN 10895639. doi: 10.1021/jp0734474.

[50] Dirac, P. A. Note on Exchange Phenomena in the Thomas Atom. *Math. Proc. Cambridge Philos. Soc.*, *26* (1930), 376–385. ISSN 14698064. doi: 10.1017/S0305004100016108.

[51] Ceperley, D. M. and Alder, B. J. Ground State of the Electron Gas by a Stochastic Method. *Phys. Rev. Lett.*, *45* (1980), 566–569. doi: 10.1103/PhysRevLett.45.566. URL https://link.aps.org/doi/10.1103/PhysRevLett.45.566.

[52] Perdew, J. P. and Zunger, A. Self-Interaction Correction to Density-Functional Approximations for Many-Electron Systems. *Phys. Rev. B*, *23* (1981), 5048–5079. doi: 10.1103/PhysRevB.23.5048. URL https://link.aps.org/doi/10.1103/PhysRevB.23.5048.

[53] Perdew, J. P.; Burke, K.; and Ernzerhof, M. Generalized Gradient Approximation Made Simple. *Phys. Rev. Lett.*, *77* (1996), 3865–3868. doi: 10.1103/PhysRevLett.77.3865.

[54] Gross, E. K. and Dreizler, R. M. Gradient Expansion of the Coulomb Exchange Energy. *Zeitschrift für Phys. A Atoms Nucl.*, *302* (1981), 103–106. ISSN 03402193. doi: 10.1007/BF01413038.

[55] Adamo, C.; Ernzerhof, M.; and Scuseria, G. E. The Meta-GGA Functional: Thermochemistry With a Kinetic Energy Density Dependent Exchange-Correlation Functional. *J. Chem. Phys.*, *112* (2000), 2643–2649. ISSN 00219606. doi: 10.1063/1.480838.

[56] Bao, J. L.; Gagliardi, L.; and Truhlar, D. G. Self-Interaction Error in Density Functional Theory: An Appraisal. *J. Phys. Chem. Lett.*, *9* (2018), 2353–2358. ISSN 19487185. doi: 10.1021/acs.jpclett.8b00242.

[57] Harvey, J. N. On the Accuracy of Density Functional Theory in Transition Metal Chemistry. *Annu. Reports Prog. Chem. - Sect. C*, *102* (2006), 203–226. ISSN 02601826. doi: 10.1039/b419105f.

[58] Stephen, P. J.; Devlin, F. J.; Chabalowski, C. F.; and Frisch, M. J. Ab Initio Calculation of Vibrational Absorption and Circular Dichroism Spectra Using Density Functional Force Fields. *J. Phys. Chem.*, *98* (1994), 11623–11627.

[59] Paier, J.; Marsman, M.; and Kresse, G. Why does the B3LYP Hybrid Functional Fail for Metals? *J. Chem. Phys.*, *127* (2007), 0–10. ISSN 00219606. doi: 10.1063/1.2747249.

[60] Krukau, A. V.; Vydrov, O. A.; Izmaylov, A. F.; and Scuseria, G. E. Influence of the Exchange Screening Parameter on the Performance of Screened Hybrid Functionals. *J. Chem. Phys.*, *125* (2006). ISSN 00219606. doi: 10.1063/1.2404663.

[61] Himmetoglu, B.; Floris, A.; De Gironcoli, S.; and Cococcioni, M. Hubbard-Corrected DFT Energy Functionals: The LDA+U Description of Correlated Systems. *Int. J. Quantum Chem.*, *114* (2014), 14–49. ISSN 00207608. doi: 10.1002/qua.24521.

[62] Anisimov, V. I.; Zaanen, J.; and Andersen, O. K. Band Theory and Mott Insulators: Hubbard U instead of Stoner I. *Phys. Rev. B*, *44* (1991), 943–954. ISSN 01631829. doi: 10.1103/PhysRevB.44.943.

[63] Lundqvist, B. I.; Andersson, Y.; Shao, H.; Chan, S.; and Langreth, D. C. Density Functional Theory Including Van Der Waals Forces. *Int. J. Quantum Chem.*, *56* (1995), 247–255. doi: https://doi.org/10.1002/qua.560560410. URL `https://onlinelibrary.wiley.com/doi/abs/10.1002/qua.560560410`.

[64] Grimme, S.; Antony, J.; Ehrlich, S.; and Krieg, H. A Consistent and Accurate Ab Initio Parametrization of Density Functional Dispersion Correction (DFT-D) for the 94 Elements H-Pu. *J. Chem. Phys.*, *132* (2010), 154104. doi: 10.1063/1.3382344.

[65] Blöchl, P. Projector Augmented-Wave Method. *Phys. Rev. B.*, *50* (1994), 17953–17979. doi: 10.1103/PhysRevB.50.17953.

[66] Kresse, G. and Furthmüller, J. Efficiency of Ab-Initio Total Energy Calculations for Metals and Semiconductors using a Plane-Wave Basis Set. *Comput. Mater. Sci.*, *6* (1996), 15–50. ISSN 09270256. doi: 10.1016/0927-0256(96)00008-0.

[67] Kresse, G. and Hafner, J. Ab Initio Molecular Dynamics for Open-Shell Transition Metals. *Phys. Rev. B - Condens. Matter Mater. Phys.*, *48* (1993), 13115–13118. ISSN 01631829. doi: 10.1103/PhysRevB.48.13115.

[68] Sattler, K. D. and Chelikowsky, J. R. Handbook of Nanophysics: Principles and Methods. *Mater. Today*, *14* (2011), 53. ISSN 13697021. doi: 10.1016/s1369-7021(11)70037-2.

[69] Schlegel, H. B. Geometry Optimization. *Wiley Interdiscip. Rev. Comput. Mol. Sci.*, *1* (2011), 790–809. ISSN 17590876. doi: 10.1002/wcms.34.

[70] *Ab Initio Molecular Dynamics*, chapter 9, pages 193–208. John Wiley & Sons, Ltd, 2009. ISBN 9780470447710. doi: https://doi.org/10.1002/9780470447710.ch9. URL `https://onlinelibrary.wiley.com/doi/abs/10.1002/9780470447710.ch9`.

[71] Koch, W. and Holthausen, M. C. *A Chemist's Guide to Density Functional Theory*. John Wiley & Sons, 2015.

[72] *DFT Calculations of Vibrational Frequencies*, chapter 5, pages 113–130. John Wiley & Sons, Ltd, 2009. ISBN 9780470447710. doi: https://doi.org/10.1002/9780470447710.ch5. URL `https://onlinelibrary.wiley.com/doi/abs/10.1002/9780470447710.ch5`.

[73] Chorkendorff, I. and Niemantsverdriet, J. W. *Concepts of Modern Catalysis and Kinetics*. WILEY-VCH Verlag GmbH & Co. KGaA, Weinheim, second, revised and enlarged edition, 2007.

[74] Henkelman, G. and Jónsson, H. Improved Tangent Estimate in the Nudged Elastic Band Method for Finding Minimum Energy Paths and Saddle Points. *J. Chem. Phys.*, *113* (2000), 9978–9985. ISSN 00219606. doi: 10.1063/1.1323224.

[75] Sanville, E.; Kenny, S. D.; Smith, R.; and Henkelman, G. Improved Grid-Based Algorithm for Bader Charge Allocation. *Journal of Computational Chemistry*, *28* (2007), 899–908. doi: https://doi.org/10.1002/jcc.20575. URL `https://onlinelibrary.wiley.com/doi/abs/10.1002/jcc.20575`.

[76] Tang, W.; Sanville, E.; and Henkelman, G. A Grid-based Bader Analysis Algorithm Without Lattice Bias. *J. Phys. Condens. Matter*, *21* (2009), 084204. ISSN 09538984. doi: 10.1088/0953-8984/21/8/084204.

[77] Lomachenko, K. A.; Borfecchia, E.; Negri, C.; Berlier, G.; Lamberti, C.; Beato, P.; Falsig, H.; and Bordiga, S. The Cu-CHA $DeNO_x$ Catalyst in Action: Temperature-Dependent NH_3-Assisted Selective Catalytic Reduction Monitored by Operando XAS and XES. *J. Am. Chem. Soc.*, *138* (2016), 12025–12028. ISSN 15205126. doi: 10.1021/jacs.6b06809.

[78] Chen, L.; Falsig, H.; Janssens, T. V.; and Grönbeck, H. Activation of Oxygen on $(NH_3–Cu–NH_3)^+$ in NH_3-SCR over Cu-CHA. *J. Catal.*, *358* (2018), 179–186. ISSN 10902694. doi: 10.1016/j.jcat.2017.12.009.

[79] Gould, H. and Tobochnik, J. *Statistical and Thermal Physics With Computer Applications*. Princeton University Press, Woodstock, Oxfordshire, 2010. P 318.

[80] Ochterski, J. W. and Ph, D. Thermochemistry in Gaussian. *Gaussian Inc Pittsburgh PA*, *264* (2000), 1–19. ISSN 13873806.

[81] Larsen, A. H.; Mortensen, J. J.; Blomqvist, J.; Castelli, I. E.; Christensen, R.; Dułak, M.; Friis, J.; Groves, M. N.; Hammer, B.; Hargus, C.; Hermes, E. D.; Jennings, P. C.; Jensen, P. B.; Kermode, J.; Kitchin, J. R.; Kolsbjerg, E. L.; Kubal, J.; Kaasbjerg, K.; Lysgaard, S.; Maronsson, J. B.; Maxson, T.; Olsen, T.; Pastewka, L.; Peterson, A.; Rostgaard, C.; Schiøtz, J.; Schütt, O.; Strange, M.; Thygesen, K. S.; Vegge, T.; Vilhelmsen, L.; Walter, M.; Zeng, Z.; and Jacobsen, K. W. The Atomic Simulation Environment—a Python Library for Working with Atoms. *Journal of Physics: Condensed Matter*, *29* (2017), 273002. URL `http://stacks.iop.org/0953-8984/29/i=27/a=273002`.

[82] Bahn, S. R. and Jacobsen, K. W. An Object-Oriented Scripting Interface to a Legacy Electronic Structure Code. *Comput. Sci. Eng.*, *4* (2002), 56–66. doi: 10.1109/5992.998641.

[83] Jørgensen, M. and Grönbeck, H. Adsorbate Entropies with Complete Potential Energy Sampling in Microkinetic Modeling. *J. Phys. Chem. C*, *121* (2017), 7199–7207. ISSN 19327455. doi: 10.1021/acs.jpcc.6b11487.

[84] Jørgensen, M.; Chen, L.; and Grönbeck, H. Monte Carlo Potential Energy Sampling for Molecular Entropy in Zeolites. *J. Phys. Chem. C*, *122* (2018), 20351–20357. ISSN 19327455. doi: 10.1021/acs.jpcc.8b05382.

[85] Niwa, M.; Katada, N.; Sawa, M.; and Murakami, Y. Temperature-Programmed Desorption of Ammonia with Readsorption Based on the Derived Theoretical Equation. *J. Phys. Chem.*, *99* (1995), 8812–8816. ISSN 00223654. doi: 10.1021/j100021a056.

[86] Katada, N.; Igi, H.; Kim, J. H.; and Niwa, M. Determination of the Acidic Properties of Zeolite by Theoretical Analysis of Temperature-Programmed Desorption of Ammonia Based on Adsorption Equilibrium. *J. Phys. Chem. B*, *101* (1997), 5969–5977. ISSN 10895647. doi: 10.1021/jp9639152.

[87] Paolucci, C.; Khurana, I.; Parekh, A. A.; Li, S.; Shih, A. J.; Li, H.; Iorio, J. R. D.; Albarracin-caballero, J. D.; Yezerets, A.; Miller, J. T.; Delgass, W. N.; Ribeiro, F. H.; Schneider, W. F.; and Gounder, R. Dynamic Multinuclear Sites Formedby Mobilized Copper Ions in NOx Selective Catalytic Reduction. *Science*, *357* (2017), 898–903.

[88] Wang, X.; Chen, L.; Vennestrøm, P. N.; Janssens, T. V.; Jansson, J.; Grönbeck, H.; and Skoglundh, M. Direct Measurement of Enthalpy and Entropy Changes in NH_3 Promoted O_2 Activation over Cu-CHA at Low Temperature. *ChemCatChem*, *13* (2021), 2577–2582. ISSN 18673899. doi: 10.1002/cctc.202100253.

[89] Campbell, C. T. Future Directions and Industrial Perspectives Micro- and Macrokinetics: Their Relationship in Heterogeneous Catalysis. *Topics in Catalysis*, *1* (1994), 353–366. doi: 10.1007/BF01492288.

[90] Stegelmann, C.; Andreasen, A.; and Campbell, C. T. Degree of Rate Control: How Much the Energies of Intermediates and Transition States Control Rates. *J. Am. Chem. Soc.*, *131* (2009), 8077–8082. doi: 10.1021/ja9000097.

[91] Bates, S. A.; Verma, A. A.; Paolucci, C.; Parekh, A. A.; Anggara, T.; Yezerets, A.; Schneider, W. F.; Miller, J. T.; Delgass, W. N.; and Ribeiro, F. H. Identification of the Active Cu Site in Standard Selective Catalytic Reduction with Ammonia on Cu-SSZ-13. *J. Catal.*, *312* (2014), 87–97. ISSN 00219517. doi: 10.1016/j.jcat.2014.01.004. URL `http://dx.doi.org/10.1016/j.jcat.2014.01.004`.

[92] Negri, C.; Selleri, T.; Borfecchia, E.; Martini, A.; Lomachenko, K. A.; Janssens, T. V.; Cutini, M.; Bordiga, S.; and Berlier, G. Structure and Reactivity of Oxygen-Bridged Diamino Dicopper(II) Complexes in Cu-Ion-Exchanged Chabazite Catalyst for NH3-Mediated Selective Catalytic Reduction. *J. Am. Chem. Soc.*, *142* (2020), 15884–15896. ISSN 15205126. doi: 10.1021/jacs.0c06270.

[93] Jones, C. B.; Khurana, I.; Krishna, S. H.; Shih, A. J.; Delgass, W. N.; Miller, J. T.; Ribeiro, F. H.; Schneider, W. F.; and Gounder, R. Effects of Dioxygen Pressure on Rates of NO_x Selective Catalytic Reduction with NH_3 on Cu-CHA Zeolites. *J. Catal.*, *389* (2020), 140–149. ISSN 10902694. doi: 10.1016/j.jcat.2020.05.022. URL `https://doi.org/10.1016/j.jcat.2020.05.022`.